Journal of Aerosol Science 188 (2025) 106612

Contents lists available at ScienceDirect

Journal of Aerosol Science

journal homepage: www.elsevier.com/locate/jaerosci

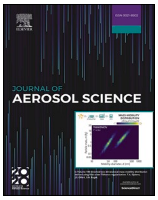

Effects of fuel sulfur content and nvPM emissions on contrail formation: A CFD-microphysics study including the role of organic compounds

S. Cantin [*], M. Chouak, F. Garnier

Department of Mechanical Engineering, École de Technologie Supérieure, University of Quebec, Montreal, QC, H3C 1K3, Canada

ARTICLE INFO

Handling editor: Chris Hogan

Keywords:
Contrail formation
CFD-Microphysics coupling
Ice crystal growth
Fuel sulfur content
Aviation emissions
Organic compounds

ABSTRACT

Aviation-induced contrails impact the climate significantly by altering atmospheric properties at cruise altitudes. Understanding the formation and evolution of ice crystals in aircraft engine plumes is essential for improving contrails prediction and mitigating their climate effects. This study introduces an innovative CFD-microphysics coupling methodology to simulate ice crystal formation in the near field of a turbofan engine plume. A 2.5D axisymmetric Eulerian-Lagrangian framework was employed, integrating gas-phase chemistry (60 reactions with 22 reactive species) and a detailed microphysical model. The model accounts for soot surface activation, condensation of organic vapors and sulfur species (H_2SO_4 and SO_3), as well as freezing and deposition processes. Results demonstrate that colder ambient temperatures (e.g., 212 K) enhance water supersaturation, accelerating ice crystal formation and growth, with soot-derived ice crystals reaching mean radii of up to 680 nm. Lower FSC increase the number of ice crystals due to the accompanying higher water supersaturation, while higher FSC promote larger ice crystals through enhanced condensation on soot particles. Organic compounds were shown to play a critical role in soot particle activation and growth, particularly under high FSC and lower temperature conditions, where they dominate the surface composition as compared to sulfur species. The soot emission index significantly influences the ice crystal number and size, with a soot emission index of 1.38×10^{13} #/kg-fuel producing the largest soot-derived ice particles due to reduced competition for available moisture. Hydrates and volatile particles exhibit peak concentrations of 10^{13} #/cm^3 under high FSC, reflecting the role of sulfuric acid in their growth.

1. Introduction

Aircraft induced cirrus (AIC) contribute to global warming by increasing cloud coverage and reflecting in/outgoing radiations. AIC are persistent condensation trails (contrails) formed behind the aircraft engine in cold and moist ambient atmospheres. Due to their warming potential, AIC have been estimated to account for approximately two-thirds of the radiative forcing attributable to the present-day aviation industry, with the remaining one-third resulting from accumulated CO_2 and NO_x emissions (Kärcher, 2018). However, estimating the impact of AIC on the energy budget using global models remains subject to significant uncertainties,

---

[*] Corresponding author.
E-mail addresses: sebastien.cantin.1@ens.etsmtl.ca (S. Cantin), mohamed.chouak.1@ens.etsmtl.ca (M. Chouak), francois.garnier@etsmtl.ca (F. Garnier).

https://doi.org/10.1016/j.jaerosci.2025.106612
Received 9 February 2025; Received in revised form 9 May 2025; Accepted 11 May 2025

Nomenclature

A	plume cross-sectional area, m^2
C_{crit}	minimum mass concentration of gaseous H_2SO_4 needed to determine whether H_2SO_4–H_2O nucleation commences, μg/m^3
C	ice shape factor
$\overline{D}_M$	geometric mean number diameter, m
D_b, D_c	bypass, core diameter, m
D_W	diffusivity of water vapor in air, m/s^2
$D_{H_2SO_4}$	diffusivity of gaseous sulfuric acid in air, m/s^2
D_{HC_j}	diffusivity of gaseous organic species *j* in air, m/s^2
d_i	particle diameter of particle i, m
D_p	particle diameter, nm
EI_M	mass-based Emission Index, mg/kg-fuel
EI_N	number-based Emission Index, #/kg-fuel
$G_{H_2SO_4}$	correction factors for condensation of gaseous sulfuric acid on soot particles
G_{HC_j}	correction factors for condensation of gaseous organic species *j* on soot particles
$J_{H_2SO_4-H_2O}$	nucleation rate in the water/sulfuric acid, particle/m^3/s
L_c	specific latent heat for condensation/evaporation, J/kg
L_d	specific latent heat for deposition/sublimation, J/kg
L, H	computational domain length, height, m
$\dot{m}_{fuel}$	fuel flow rate, kg/s
m_{water}, m_{ice}	condensed mass of water, ice on soot particles, kg
m_{sulf}, m_{org}	condensed mass of sulfur, organic species on soot particles, kg
$M_{H_2SO_4}$	molar mass of sulfuric acid, kg/mol
M_{HC_j}	molar mass of organic species *j*, kg/mol
N	particle number concentration, #/cm^3
N_{com}	number of particles per computed particle
N_D	dilution ratio
N_{tot}	total number concentration of particles, #/cm^3
n_i	number concentration of the computational particle i, #/cm^3
P_W	vapor pressure of water vapor, Pa
$P_{H_2SO_4}$	vapor pressure of sulfuric acid, Pa
P_{HC_j}	vapor pressure of organic species j, Pa
P_W^{sat}	saturation vapor pressure of water vapor, Pa
P_I^{sat}	saturation vapor pressure of ice, Pa
$P_{H_2SO_4}^{sat}$	saturation vapor pressure of sulfuric acid, Pa
$P_{HC_j}^{sat}$	saturation vapor pressure of organic species *j*, Pa
P_b, P_c	bypass, core-pressure inlet, Pa
P_a	far-field ambient pressure, Pa
RH	relative humidity with respect to liquid water
S_w^m	mean saturation of water of particles
T	gas phase temperature, K
T_{frz}	freezing temperature, K
T_a	far-field ambient temperature, K
T_b, T_c	bypass, core temperature inlet, K
$\dot{T}$	plume cooling rate, K/s
T_p^m	mean temperature of particles, K
R	universal gas constant, J/mol/K
r_d	radius of a dry soot particle, m
R_W	the specific gas constant of vapor, J/kg/K
r_p	radius of particles, m
r_p^m	mean particle radius, m
Sc	gas Schmidt number
Sc_t	turbulent gas Schmidt number
t	time, s
V	velocity of the aircraft, m/s
$\overline{\dot{w}}_{chem}$	coupling term for mass transfer for chemical reaction, kg/m^3/s

$\overline{w}_{adsk}$	coupling term for mass transfer for activation, $kg/m^3/s$
$\overline{w}_{condk}$	coupling term for mass transfer for condensation of vapor, $kg/m^3/s$
$\overline{w}_{depo_k}$	coupling term for mass transfer for deposition of ice, $kg/m^3/s$
$\overline{w}_{nuclk}$	coupling term for mass transfer for nucleation of droplet, $kg/m^3/s$
X_k	molar fraction of gaseous species k
$\widetilde{y}_k$	mean mass fraction of species k

Greek Letters

α_W	activity of water in the soot coating liquid mixtures
$\alpha_{H_2SO_4}$	activity of sulfuric acid in the soot coating liquid mixtures
α_{HC_j}	activity of organic species *j* in the soot coating liquid mixtures
β_m, β_t	correction terms for mass and heat term
β_v, β_k	transitional correction factors
Δx	mesh cell size, m
Δt	time step, s
$\Theta_{aq,i}$	activated aqueous fraction of surface for the particle i
$\Theta_{non-aq,i}$	activated non-aqueous fraction of surface for the particle i
$\kappa_{aq/non-aq,i}$	Kelvin factor in the particle coatings liquid mixture for the particle i
λ	conductivity of air, W/m/K
μ_g	dynamic viscosity of gas, Pa.s
$\mu_{t,g}$	turbulent dynamic viscosity of gas, Pa.s
ρ	air density within the exhaust plume, kg/m^3
$\overline{\rho}_g$	mean gas mixture density, kg/m^3
σ	geometric standard deviation
Φ_{act}, Φ_{frz}	activation and freezing fractions of particles

Acronyms and abbreviations

DLR	Deutsches Zentrum für Luft-und Raumfahrt
FSC	fuel sulfur content
ICAO	International Civil Aviation Organization
NASA	National Aeronautics and Space Administration
PDF	probability density function
ppm	parts per million

particularly with respect to ice crystal number densities in young contrails (Lee et al., 2020), and uncertainties of around 20 % in AIC radiative forcing (RF). Given the constant annual increase in aviation traffic, estimated at around 3.6 % per year over the next 20 years (Airbus, 2023), there is a strong need to develop reliable decision-making tools that can provide a more precise characterization of the microphysical properties of young contrails. This will, in turn, enhance the accuracy of persistent contrail and AIC atmospheric impact assessments.

The formation of contrails depends on complex thermodynamic, microphysical and chemical processes within the aircraft exhaust plume, and typically occurs within the first few seconds of plume mixing. Aircraft plumes consist of three primary aerosol components: non-volatile particulate matter (nvPM), volatile particulate matter (vPM) and entrained ambient particles. Non-volatile particulate matter (nvPM), primarily composed of soot particles, initially exhibits hydrophobic characteristics (Mikhailov et al., 2001). These particles can become activated through interactions with chemical species such as sulfuric acid (H_2SO_4), trioxide (SO_3), or volatile organic compounds (VOCs) (Wong et al., 2014). As the plume undergoes dilution and cooling, the activated soot particles undergo a phase transition, first by forming water droplets through the condensation of water vapor, and subsequently by transforming into ice crystals via homogeneous ice nucleation at temperatures around 235 K (Kärcher et al., 2015). The ice crystals continue to grow through ice deposition, as long as the exhaust air continues to be supersaturated with respect to ice (Gorbunov et al., 2001). The water/ice supersaturation in the plume and the temperature at which these phase transitions occur depend on the physicochemical properties of the condensation nuclei (CN) (Ponsonby et al., 2023) and the characteristics of their liquid coatings (Li et al., 2024) (i.e., the water activity (Bier et al., 2023)). These parameters are further influenced by the plume cooling conditions, as discussed by Kärcher et al. (1996). The physicochemical properties of liquid coatings—including the effect of organic matter on the fractional soot coating—might also affect the growth of ice crystals (Fritz et al., 2020). Since contrail ice formation depends on the CN availability and properties, a comprehensive understanding of the nature of CN present in aircraft exhaust plumes is essential.

In contrast to non-volatile particulate matter (nvPM), volatile particulate matter (vPM) primarily consists of ultrafine aqueous particles that form within the aircraft exhaust after sufficient cooling. vPM comprises an organic fraction originating from unburned fuel and engine lubrication oil hydrocarbons, as well as an inorganic fraction predominantly composed of sulfates (Timko et al., 2010a, 2010b). These sulfates are formed through the oxidation of sulfur compounds present in the fuel (via SO_2 and SO_3). Downstream of the engine exit plane, vPM can undergo coagulation with nvPM or serve as nuclei for the formation of new particles. The predominance of one process over the other depends on multiple factors, including engine thrust (Yu et al., 2019), fuel type (Rojo et al., 2014), and atmospheric conditions (Kärcher, 2018). Subsequently, these vPM-based particles can become frozen through homogeneous ice nucleation. Additionally, ambient aerosols can be entrained within the aircraft plume, leading to the formation of water droplets and ice crystals (Rojo et al., 2014). However, the influence of ambient aerosols becomes particularly relevant when studying alternative/hydrogen liquid fuels, or in cases where the plume duration exceeds around 5 s when using kerosene fuel (Rojo et al., 2014).

Several studies have been conducted on contrail formation in aircraft plumes. In one such work, 3D Computational fluids dynamics (CFD) models were employed to provide a detailed representation of plume dynamics with either Large Eddy Simulations (LES) (Garnier et al., 2014; Paoli et al., 2013) or Reynolds-Averaged Navier-Stokes (RANS) (Cantin et al., 2021; Guignery et al., 2012; Khou et al., 2016) approaches without incorporating any complex chemistry or detailed microphysics. On the other hand, box models can be coupled in a one-way coupling either with 3D CFD (trajectory box model (0D)) or with averaged plume dilution (1D). In the latter, 1D models are generally equipped with detailed microphysical and chemistry schemes. For example, Kärcher (1998) developed a coupled microphysical-chemical trajectory box model that included $HNO_3/H_2SO_4/H_2O$ liquid aerosols and soot particles. The model accounted for main contrail microphysical processes such as activation by species, coagulation, binary homogeneous nucleation and hetero-molecular condensation. For instance, species such as H_2O, H_2SO_4, SO_3, and HNO_3 were involved in the formation and growth of aerosols. However, organic emissions that may play an important role in ice crystal formation were not included (Gao & Kanji, 2022). Later, Yu and Turco and Kärcher (1999) developed a microphysical model that accounted for formation of new particles, including sulfuric acid ion clusters and organic compounds (Yu and Turco and Kärcher, 1999). By employing a kinetic collision model to simulate aerosol formation, the model successfully reproduced the evolution of Apparent Emission Indices (AEI) for volatile particles, aligning well with in-flight measurements (Kärcher et al., 2000). The significant contribution of organic species emitted by aircraft engines to the formation of ultrafine volatile particles was highlighted, especially for low sulfur fuel contents. Kärcher & Yu (Karcher & Yu, 2009) examined the sensitivity of the emitted soot particle number, while Rojo et al. (2014) explored the impact of alternative jet fuel use on induced ice particles. In later studies, only two types of organic species were considered, namely, water-soluble and water-insoluble organic compounds, which may not be representative of the main organic compound families (e.g., carbonyls, aromatics, and alcohol (Kılıç et al., 2017)) at the nozzle exit, whose physical properties differ significantly. A conceptual model was proposed by Kärcher et al. (2015) to characterize contrail formation in jet plumes from water vapor emissions. The model provided a comprehensive description of the near-field growth mechanism by incorporating key features of contrail microphysics, primarily focusing on the activation of soot and ambient particles through an analytical parameterization derived from Köhler theory. Overall, modeling studies on ice particle formation in aircraft wakes have significantly enhanced our understanding of contrail microphysical processes by employing refined growth mechanisms involving the solubility effect, for example. However, the role of organic species in contrail formation remains underexplored and inadequately understood, and thus the need for further investigations. As pointed out by Yu and Miake-Lye (2024), their consideration in contrail modeling could change the uptake of other gases as well as the activation of particles for ice crystal formation.

In the last decade, improvements in computing technologies and numerical methods progressed to a level enabling the effective modeling of contrail formation, including complex interactions between turbulent plume dynamics, chemical reactions, and detailed microphysics. For a comprehensive characterization of ice crystal properties, some authors have integrated the 3D LES approach with an offline detailed microphysics modeling, either incorporating a parameterized solubility model (Bier et al., 2023; Bier, Unterstrasser, & Vancassel, 2021) or accounting for interspecies interactions affecting solubility within a box model (Vancassel, Mirabel, & Garnier, 2014). Regarding the online coupling approach, Lewellen (2020) used a 3D LES model incorporating a detailed microphysical model using a hygroscopicity parameter for particles solubility, and which considered an appropriate microphysical pathway consistent with the Schmidt Appleman criterion. Exhaust particles, including soot, volatile and ambient particles, which could possibly initiate water droplets and form ice crystals, were modeled in a Eulerian approach assuming a monodisperse (or at best bi-disperse) size distribution. This approach could fall short when it comes to capturing the Kelvin effect-driven competition among aerosol particles of varying sizes, which could potentially result in overly narrow ice crystal size spectra. Additionally, the physicochemical properties of liquid layers on soot particle coatings, particularly the Raoult effect (solute), which may affect the transition to water droplets and ice crystals, are not accounted for. These liquid layers evolve with plume age by absorbing condensable gases, thereby altering the particle surface solubility. Khou et al. (Khou et al., 2016) used a RANS approach to investigate the near-field contrail behind a realistic twin-jet Boeing 737 geometry using simplified coplanar exits for both fan and core nozzle flows. While their model accounted for the detailed gas phase chemistry (23 reactive species) and advanced microphysics of both soot and ice particles, with activation based on chemical composition, it does not include the homogeneous freezing of soot particles or the formation and growth of volatile sulfate particles, which can increase the ice crystal number.

In this study, our initial microphysical model, PAMMAP (PArticle-based Microphysical Model for Aircraft Plumes), developed for aerosol formation at ground level (Cantin, Chouak, & Garnier, 2024), was extended to account for ice crystal formation at cruise level. This paper proposes a detailed microphysical model incorporating multicomponent organic and sulfuric acid compounds for ice contrail formation. To the authors' knowledge, no study has investigated the formation and growth of volatile sulfate aerosols in a CFD-microphysics online coupling framework. The paper is organized as follows. Section 2 provides a model description of the aerosol and ice crystals formation in near-field aircraft plumes. Section 3 presents the governing equations of the fluid dynamics, particle motion, gas phase chemistry, and the aerosol microphysics. Section 4 describes the numerical methods, including the characterization of organic compounds at the nozzle exit and the grid configuration. Finally, Section 5 presents the analysis of ice crystal properties regarding the effects of ambient temperature, FSC and soot emissions levels.

2. Model description of ice crystals formation

The modeling approach used for the formation of ice particles and aerosols is illustrated in Fig. 1. The nozzle exit flow from the turbofan engine at cruise consists of two jets: a hot core flow and a surrounding cold bypass flow. The bypass jet contains ambient moist air that is accelerated by the engine fan, while the core jet drives the fuel combustion products composed of gaseous emissions laden with primary aerosols (soot particles). Both jets mix with the freestream (ambient) cold and moist air. Freshly emitted soot particles are initially hydrophobic (non-activated). Their surfaces can be activated by sulfuric acid or water-soluble organic species rendering them hydrophilic (aqueous), or even by water-insoluble organic species to maintain their hydrophobic (non-aqueous) nature. Consequently, sulfuric acid and organic liquid layers can form through vapor condensation on activated soot particles. In addition to gaseous adsorption on soot, activation by collisions of sulfuric acid droplets with soot surfaces is also considered. As the plume dilutes and cools, activated soot particles form water droplets through water vapor condensation, followed by ice crystal formation via homogeneous freezing at approximately 235 K (Kärcher et al., 2015). Ice crystals subsequently grow by deposition as long as the exhaust air remains supersaturated with respect to ice. New liquid particles are formed via binary homogeneous nucleation of H_2SO_4-H_2O clusters. In addition, droplets tend to coagulate due to their high concentration in the exhaust plume. Given the relatively low ambient temperature at cruise level, condensation of gaseous species such as water, sulfuric acid, and organic compounds onto droplets is likely to occur. The proposed model accounts for vapor condensation around sulfuric acid droplets, which leads to multi-component sulfuric acid droplets. Lastly, ice crystals can form from these droplets via homogeneous freezing and subsequently grow through ice deposition.

3. Mathematical equations

3.1. Gas phase flow and dispersed phase

The mean flow of the exhaust jet is assumed to be axisymmetric and compressible. Therefore, the unsteady Reynolds-averaged Navier-Stokes (RANS) equations expressing the conservation of the gas phase global mass, momentum, and energy were solved in cylindrical coordinates (O, $\vec{r}$, $\vec{z}$) (CD-Adapco, 2021). To compute the mixture composition in the gas phase ($\Phi_g = \sum_k \bar{y}_k \Phi_k$), the mass fractions of species ($\bar{y}_k$) were derived with Eq. (1) defined as follows:

$$\frac{\partial(\bar{\rho}_g \bar{y}_k)}{\partial t} + \frac{\partial(\bar{\rho}_g \bar{u}_j \bar{y}_k)}{\partial r_j} = \frac{\partial}{\partial r_j}\left(\left(\frac{\mu_g}{Sc} + \frac{\mu_{t,g}}{Sc_t}\right)\frac{\partial \bar{y}_k}{\partial r_j}\right) + \bar{\dot{w}}_{chemk} + \bar{\dot{w}}_{adsk} + \bar{\dot{w}}_{condk} + \bar{\dot{w}}_{depo_k} + \bar{\dot{w}}_{nuclk}, \quad (1)$$

Equation (1) translates the mass conservation of species which is governed by their average mass fraction $\bar{y}_k$, their diffusion coefficient in the mixture D_k, and the average mixture gas density $\bar{\rho}_g$. The rate of mass transfer $\bar{\dot{w}}_{chemk}$ is a function of chemical reactions, while $\bar{\dot{w}}_{adsk}$, $\bar{\dot{w}}_{condk}$, $\bar{\dot{w}}_{depo_k}$ and $\bar{\dot{w}}_{nuclk}$ are functions representing the one-way coupling with the microphysics modeling of adsorption, condensation, ice deposition and nucleation of gaseous species, respectively. A detailed description of these coupling terms is available in (Cantin et al., 2024). The variables Sc and Sc_t denote the Schmidt number and the turbulent Schmidt number, taken as being equal to 1 and 0.9 (Cantin et al., 2021), respectively. The eddy viscosity term introduced by the Boussinesq approximation was modeled using the Realizable k-ε model (CD-Adapco, 2021), selected based on prior validation results comparing three eddy-viscosity models with experimental data for compressible coaxial jets (Cantin et al., 2021).

The major gaseous emissions from aircraft engines are carbon dioxide CO_2 and water vapor (H_2O). Minor species are nitrogen oxides (NO_x), carbon oxide (CO), hydrocarbons, and organic compounds. Sulfur oxides (SO_x) are also present due to the FSC. Many chemical interactions occurring between NO_x, HO_x, and SO_x in aircraft engine plumes need to be characterized. For instance, SO_x products are important as they act as aerosol precursors, which promote homogenous nucleation and form volatile sulfate aerosols. A kinetic reaction scheme based on the works of Kärcher et al., (1996) and Khou et al. (2016) was implemented in the CFD code Star-CCM+. The mass reaction rates of chemical species were assessed with the Arrhenius law. However, this scheme does not include any hydrocarbon chemistry since the reactions of organic compounds occur at minute timescales, which is too long to affect conditions in our period of interest (Garmory, Britter, & Mastorakos, 2008). The scheme consists of 60 reactions, with 22 reactive species, including NO_x, SO_x, HO_x, and 29 non-reactive species, including organic compounds. The choice of organic compounds will be

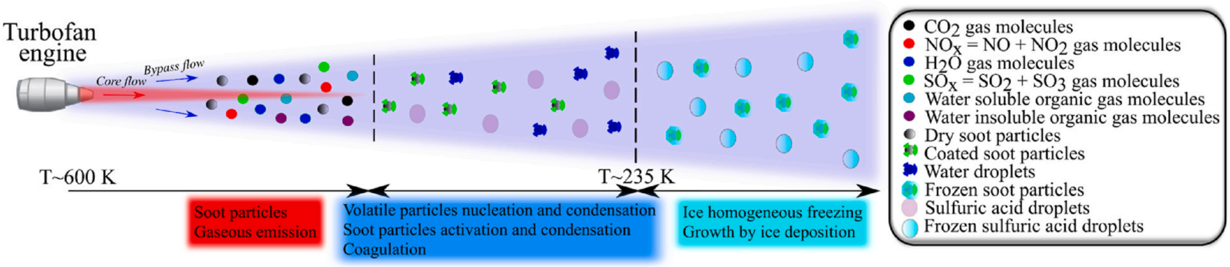

Fig. 1. 2D Scheme of the exhaust jet from a turbofan engine with ice crystals formation.

discussed later.

A Lagrangian tracking method was used for the dispersed phase to track the particle motion. As the number density of physical soot particles is relatively high, with a number-based emission index of around 10^{14} #/kg-fuel at the exhaust nozzle plane (Wey et al., 2007), a modeling simplification was required to reduce the simulation time. Therefore, computational particles were considered as spheres of radius r_p, with each representing N_{com} physical particles (Schröder, Karcher, et al., 2000). Numerically, soot particles and liquid droplets are treated as passive tracers by neglecting their drag and gravitational forces (Garnier et al., 2014), allowing them to share the same velocity as the carrier phase.

3.2. Microphysical model for contrail formation

This section provides an overview of the detailed microphysical model, PAMMAP. The model addresses key processes such as the homogeneous binary nucleation of H_2SO_4/H_2O clusters, the coagulation of liquid aerosols and soot particles, and the activation and condensation on soot particle surfaces. More details regarding the original model can be found in the previous paper (Cantin et al., 2024). In that study, the model was further extended to incorporate the formation of ice particles at cruise level.

3.2.1. Homogeneous binary nucleation and coagulation of sulfuric acid-water droplets

New liquid droplets can form through binary homogeneous nucleation (BHN) of sulfuric acid and water. Before becoming droplets, hydrated clusters can nucleate if their radius is smaller than their critical radius computed in the model. Given the range of ambient conditions relevant to an aircraft plume, the nucleation rate $J_{H_2SO_4-H_2O}$ (number of new embryos formed per second and per cubic meter) in the water/sulfuric acid mixture was calculated based on the cluster size, composition, and nucleation rate, using the parameterization from Määttänen et al. (2018). The H_2SO_4–H_2O nucleation rate is highly dependent on the temperature, relative humidity, and H_2SO_4 concentration. The following empirical criterion (Casati et al., 2007; Seinfeld & Pandis, 2016) is used to determine whether H_2SO_4-H_2O nucleation commences:

$$C_{crit} = 0.16\,\exp(0.1\,T - 3.5\,RH - 27.7), \tag{2}$$

where RH is the relative humidity on a scale ranging from 0 to 1, and T is the gas phase temperature. When the gas phase concentration of H_2SO_4 exceeds C_{crit}, the nucleation of H_2SO_4–H_2O embryos begins. The model then accounts for the coagulation and self-coagulation of liquid droplets as described in (Cantin et al., 2024).

3.2.2. Activation of soot surfaces

Freshly emitted soot particles from gas turbine engines are bare and initially hydrophobic. The activation of soot surfaces relies on the adsorption of vapor species, which is essential for the subsequent vapor condensation on soot. Activation of soot surfaces can occur through interactions with sulfuric acid or water-soluble organic species, resulting in hydrophilic (aqueous) properties, or with water-insoluble organic species, leading to hydrophobic (non-aqueous) characteristics (Wong et al., 2014). Our model accounts for both activation schemes. One should note that water is not directly involved in this activation process due to the perceived difficulty of water adsorption on hydrophobic soot surfaces (Brown et al., 1996), especially in the presence of sulfuric acid (Kärcher, 1998). Additionally, apart from gaseous adsorption on soot, activation can also occur through collisions of nucleated liquid droplets with soot surfaces, a process known as scavenging (Wong et al., 2015). This scavenging process is modeled using the Brownian coagulation between scavenged liquid droplets and soot particles. Ultimately, the activated soot surface fraction can be quantified by $\Theta_{aq,i}$ for aqueous species and $\Theta_{non-aq,i}$ for non-aqueous species.

3.2.3. Liquid condensation growth of sulfuric acid, organics and water vapors on soot particles and droplets

Once soot particles are activated, condensation of vapors can also occur on their surfaces. Species such as water, sulfuric acid, and water-soluble organics can condense on the aqueous (hydrophilic) part of the surface, while only water-insoluble organics can condense on the non-aqueous (hydrophobic) part. The total mass of sulfuric acid, and organic species j on a soot particle i due to condensation is calculated by:

$$\left.\frac{dm_i}{dt}\right|_{cond,s} = 4\pi\, D_{H_2SO_4}\, r_p\, G_{H_2SO_4}\, \Theta_{aq,i} \left(\frac{P_{H_2SO_4} - \kappa_{aq,i}\alpha_{H_2SO_4}P^{sat}_{H_2SO_4}}{RT}\right) M_{H_2SO_4}, \tag{3}$$

$$\left.\frac{dm_i}{dt}\right|_{cond,HC_j} = 4\pi\, D_{HC_j}\, r_p\, G_{HC_j}\, \Theta_{aq/non-aq,i} \left(\frac{P_{HC_j} - \kappa_{aq/non-aq,i}\alpha_{HC_j}P^{sat}_{HC_j}}{RT}\right) M_{HC_j}, \tag{4}$$

where $D_{H_2SO_4}$ and D_{HC_j} are the diffusivities of the vapor phase sulfuric acid and organic species j in air. $P_{H_2SO_4}$ and P_{HC_j} are the vapor pressure of sulfuric acid and organic species j. $P^{sat}_{H_2SO_4}$ and $P^{sat}_{HC_j}$ are the saturation vapor pressure of sulfuric acid and organic species j. $\kappa_{aq/non-aq}$ denotes the Kelvin factor of soot particles. $\alpha_{H_2SO_4}$ and α_{HC_j} are the activity of sulfuric acid and organic species j in the soot coating liquid mixtures. $G_{H_2SO_4}$ and G_{HC_j} are the correction factors for condensation of each species on soot particles (Pruppacher & Klett, 1998). $M_{H_2SO_4}$ and M_{HC_j} are the molar mass of sulfuric acid and organic species j, and R denotes the universal gas constant.

For water vapor, the mass and size change of a single particle due to condensation/evaporation effects can be expressed by a diffusion law as described by (Kulmala, 1993):

$$\left.\frac{dm_i}{dt}\right|_{cond,w} = \frac{4\pi R_p \Theta_{aq,i}\left(P_W - \kappa_{aq}\alpha_W P_W^{sat}\right)}{\frac{R_W T}{D_W \beta_m} + \frac{P_W L_c^2}{R_W \lambda T^2 \beta_t}} \tag{5}$$

where P_W is partial vapor pressure and P_W^{sat} is the equilibrium saturation vapor pressure of liquid water over a flat surface, κ_{aq} describes the exponential Kelvin term that includes the liquid mixture properties, followed by the activity of water α_W. L_c denotes the specific latent heat for condensation/evaporation, $\lambda,$ the conductivity of air; D_W the binary diffusion coefficient of water vapor in air, and R_W is the specific gas constant of vapor. The terms β_m and β_t represent the transitional correction factors calculated according to (Fuchs & Sutugin, 1971). Regarding the growth of homogeneous liquid droplets, the governing equations are similar to those describing the condensation growth for soot particles, i.e., Eqs. (3)–(5). However, the activated surface fraction of droplets is assumed to be $\Theta_{aq/non-aq,i} = 1$ since droplets do not require any form of activation.

3.2.4. *Ice homogeneous freezing*

As the plume dilutes and cools down, water droplets formed from soot particles or homogeneous liquid droplets can become ice crystals if the homogenous freezing temperature is reached. The homogeneous freezing temperature T_{frz} of super-cooled droplets with radius r_p is calculated according to (Bier et al., 2021; Kärcher et al., 2015) as follows:

$$T_{frz}\left(r_p, \dot{T}\right) = \frac{1}{a_1}\left[\ln\left(\frac{3\times 10^{-6} a_1 \dot{T}}{4\pi\left(r_p^3 - r_d^3\right)}\right) - a_2\right] \tag{6}$$

where $a_1 = 3.574\ \mathrm{K}^{-1}$ and $a_2 = 858.72$ are empirical constants r_d is the dry particle radius, and $\dot{T}$ is the cooling rate of the jet plume. This method is suitable for a strong cooling situation typically occurring in a jet plume. The liquid solution of the droplet, which is related to the activity of water a_W affects the homogeneous freezing temperature T_{frz}, where T_{frz} decreases with decreasing a_W. To account for that phenomena, the model of (Bier et al., 2023) was considered to take into account the solution effect in computing the homogeneous freezing temperature.

3.2.5. *Deposition ice crystal growth of water vapor*

The mass change of a single ice crystal following homogeneous freezing of ice on its surface is computed as follows (Mason, 1971):

$$\left.\frac{dm_i}{dt}\right|_{depo,I} = \frac{4\pi C r_p\, D_W \beta_v^{-1}\, \Theta_{aq,i}\left(P_W - \kappa_{aq}\alpha_W P_I^{sat}\right)}{\frac{D_W \beta_v^{-1} L_d P_I^{sat}}{\lambda \beta_k^{-1} T\left(\frac{L_d}{R_W T} - 1\right)} + R_W T} \tag{7}$$

where P_I^{sat} is the equilibrium saturation vapor pressure of ice over a flat surface, and L_d is the specific latent heat for deposition/sublimation. In our study, the shape factor C was set to unity by assuming spherical ice crystals typically observed in young contrails (Schröder, Brock, et al., 2000). The detailed calculation of the transitional correction factors β_v and β_k is decribed in (Bier et al., 2021).

4. Methods

4.1. *Characteristics of the gaseous organic compounds at engine exhaust*

Organic gaseous species are important for the activation and growth of soot particles as well as the growth of liquid droplets. However, the speciation of organic species emitted at the nozzle exit of a cruising aircraft engine is challenging to determine accurately (Slemr et al., 2001). Recent field measurements by Kılıç et al. (2017) characterized organic emissions at 1.5 m behind different aircraft engines, and thus helped identify gaseous organic species for engine power settings ranging from 4 % to 100 %. Given the variety of organic species emitted from aircraft gas turbine engines—approximately 200 gaseous organics measured in Kılıç et al. (2017)—it was

Table 1

List of organic surrogate species for 65 % engine power.

Families of HC species	Organic Species	EI_m (mg.kg-fuel^{-1})	Percentage of the total EI_m of organic species	Percentage of the total family EI_m of soluble/insoluble organic species
Acids	$C_2H_4O_2$, CH_2O_2	26.45	20.4	100/0
Aliphatics	C_3H_4	2	1.5	0/100
Aromatics	$C_{14}H_{10}$, $C_{16}H_{10}$, $C_{20}H_{12}$, $C_{22}H_{12}$, C_7H_8, C_8H_{10}, C_9H_{12}, $C_{10}H_{14}$	33.31	25.7	0/100
Carbonyls	C_3H_6O, $C_3H_6O_2$, C_2H_4O, $C_3H_4O_2$, $C_4H_2O_3$, C_4H_8O, $C_4H_4O_3$, $C_4H_6O_2$, CH_2O, $C_6H_{10}O$, $C_5H_8O_2$	38.85	30	100/0
O-containing	C_2H_2O, $C_8H_4O_3$	6.85	5.3	78/22
Non aromatics	C_4H_8, C_4H_6, C_6H_{10}, C_5H_8, C_7H_{12}	22.2	17.1	0/100

impractical to include all emitted organic species in our model simulations. As a result, we considered 70 % of the total mass-based emission index (EI_m), representing 25 organic species at 65 % engine power (cruise regime). Additionally, since our goal was to select typical organic surrogate species covering a broad volatility range and allowing for interactions with aircraft-emitted soot particles, we had to consider volatile organics having sufficiently low vapor pressures to allow for condensation onto soot particles. Consequently, we added four extra organic species, namely, $C_{14}H_{10}$, $C_{16}H_{10}$, $C_{20}H_{12}$ and $C_{22}H_{12}$ to obtain a more representative set of organic compounds in a plume, as per (Cantin et al., 2024; Wong et al., 2014). The emission indices for these species were taken from (Jathar et al., 2012; Presto et al., 2012). A list of organic surrogate species selected for our modeling work is provided in Table 1.

4.2. Aero-thermodynamics conditions

The engine was assumed to operate under typical cruise conditions, including in terms of both atmospheric parameters and engine emissions, as well as exhaust gas temperature. The cruise ambient conditions were set with a temperature of 218.8 K, a pressure of 23,842 Pa, and a cruise speed of 237 m/s (Mach 0.8). The molar fraction of water vapor was set to 9.55×10^{-5}, resulting in a relative humidity with respect to ice of 100 %. The engine core flow and bypass flow properties of the jet engine are listed in Table 2. The exhaust aerothermodynamic conditions for the core and bypass flows were computed using *GasTurb* (Kurzke, 2004).

Molar fractions for the 22 reactive species in the core flow and background air were taken from (Garnier et al., 1997), with bypass stream species initialized as background values. It should be noted that the initial molar fraction of SO_2 at the nozzle core exhaust ($X_{SO_2} = 5.8 \times 10^{-6}$) corresponds to a FSC of 700 ppm. A verification using the reaction mechanism of Khou (2016) confirmed that the evolution of the molar fraction of species up to 1000 m behind the engine jet closely matches the author's results, using a test case for the CF6-80 turbofan engine (Kärcher and Hirschberg and Fabian, 1996).

Two types of aerosols were modeled in this study: soot particles and H_2SO_4/H_2O clusters/liquid droplets. Background particles were excluded from the model, as their influence is more significant for aircraft with low soot or soot-free emissions, such as those using liquid hydrogen propulsion (Bier et al., 2023). Soot particles are directly emitted from the engine core, while liquid particles form from hydrated clusters in the exhaust plume. Clusters become liquid particles when they exceed the critical radius computed following (Määttänen et al., 2018). For soot particles, a poly-disperse distribution was considered, treating all emitted particles as spheres with a different radius r_p. The emission indices of soot particles in number EI_n at cruise flight conditions was estimated using the methodology proposed by (Ahrens et al., 2022), resulting in $EI_n = 1.38 \times 10^{14}$ #/kg-fuel, based the International Civil Aviation Organization (ICAO) Emission Databank [26] for the CFM56-5B3 engine. The geometric mean diameter $\overline{D}_M$ and the geometric standard deviation σ of the soot distribution were found to be 26 nm and 1.73, respectively, from experimental measurements for a $\sim$ 65 % engine power (Lobo et al., 2015). For H_2SO_4/H_2O clusters, the mean particle radius was set to 0.277 nm (Kärcher et al., 2007) with a geometric standard deviation of 1.6 (Kärcher and Hendricks and Lohmann, 2006). The initial profile distribution for soot particles and H_2SO_4/H_2O clusters was computed as a lognormal (Jacobson, 2005) as follows:

$$n_i = \frac{N_{tot}\Delta d_i}{d_i\sqrt{2\pi}\ln(\sigma)}\exp\left(\frac{-ln^2(d_i/\overline{D}_M)}{2\,ln^2(\sigma)}\right) \tag{8}$$

where N_{tot} is the total number concentration of particles, n_i is the number concentration of the computational particle i, d_i is the particle diameter, $\overline{D}_M$ is the geometric mean number diameter, and σ is the geometric standard deviation.

4.3. Computational domain and grid

A realistic CFM56-5B3 engine geometry, including both bypass and core flows, was used. The flow was assumed to be axisymmetric, leading to a 2.5D axisymmetric representation of the engine nozzle, as shown in Fig. 2. The nozzle duct from the inlet to the exit was modeled for both bypass and core outlets to promote the boundary layer development adjacent to the jet. The bypass and core nozzle diameters were $D_c = 0.638$ m and $D_b = 1.755$ m, respectively. The computational domain was rectangular, with a length $L = 148\,D_b$ (=260 m) and height $H = 20\,D_b$. Three inlet sections were used: a freestream pressure inlet (P_a, T_a), a bypass pressure inlet (P_b, T_b), and a core pressure inlet (P_c, T_c). No-slip adiabatic conditions were applied on engine walls, a slip condition was used for the upper boundary, while a pressure outlet condition was set for the far-field boundary.

Table 2
CFM56-5B3 exhaust properties at cruise flight conditions.

	Parameters	Values
Core flow	Total Temperature (K) T_c	717
	Total Pressure (Pa) P_c	48,263
	Soot number emission index EI_N (#/kg-fuel)	1.38×10^{14}
	Soot $\overline{D}_M$ (nm)/σ_g	26/1.73
	H_2SO_4/H_2O clusters $\overline{D}_M$ (nm)/σ	0.554/1.6
	Molar fraction of H_2O X_{H_2O}	3.6×10^{-2}
	Molar fraction of SO_2 X_{SO_2}	5.8×10^{-6}
Bypass flow	Total Temperature (K) T_b	294
	Total Pressure (Pa) P_b	56,000

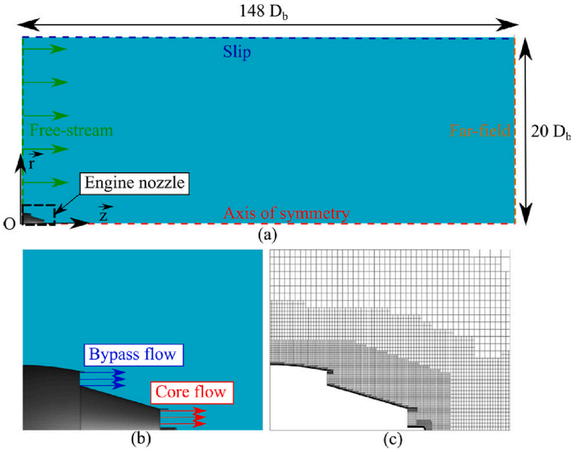

Fig. 2. Computational domain and grid for the CFM56-5B3: (a) 2D domain view, (b) nozzle geometry, and (c) mesh around the engine wall.

A grid convergence study for the gaseous phase was performed using three grids: coarse (45,000 cells), medium (90,000 cells), and fine (268,000 cells). Mean errors in the inner shear layer for static temperature, water vapor mass fraction, and axial velocity were below 1 % between the medium and fine grids. Discretization errors in the inner shear layer for static temperature, water vapor mass fraction, and axial velocity were estimated using the GCI method (Celik et al., 2008) at a probe point ($r = 0.5\ D_b$, $y = 2\ D_b$). Results indicated sufficiently low errors (<1 %) with the medium grid, which was retained for computations.

The medium grid primarily consists of hexahedral and prismatic elements, as shown in Fig. 2-c. Refinement blocks were used in the core and bypass flow ducts and near the engine nozzle ($<20\ D_b$) to capture high gradients in the shear layer ($\Delta x = 0.03\ D_b$). The mesh in the far field is coarser, with cells about $\Delta x = 0.15\ D_b$, and cell anisotropy in the duct is ($\Delta x = 0.02\ D_b$). Near-wall refinement ensures a maximum y^+ of 10, resolving the boundary layer with a wall law function.

To solve the equations governing particle activation, growth, and surface coverage change of the microphysical model, a fourth-order Runge-Kutta scheme was employed. The microphysical module was implemented as a user-defined function in the commercial CFD code STAR-CCM + v2020.2. The methodology for coupling with the CFD solver was detailed in (Cantin et al., 2024). A second-order upwind scheme was employed for spatial discretization, while time integration was performed using a second-order implicit backward differentiation formula. For time discretization, a time step of $\Delta t = 10^{-3}$ s was used, ensuring that the Courant–Friedrichs– Lewy number did not exceed a value of 3 along the plume.

5. Results and discussion

This section presents the results of contrail formation simulations for a CFM56-5B3 engine under cruise flight conditions. Simulations were carried out at four different ambient temperatures (212, 218.8, 223, and 225K) with a relative humidity with respect to ice

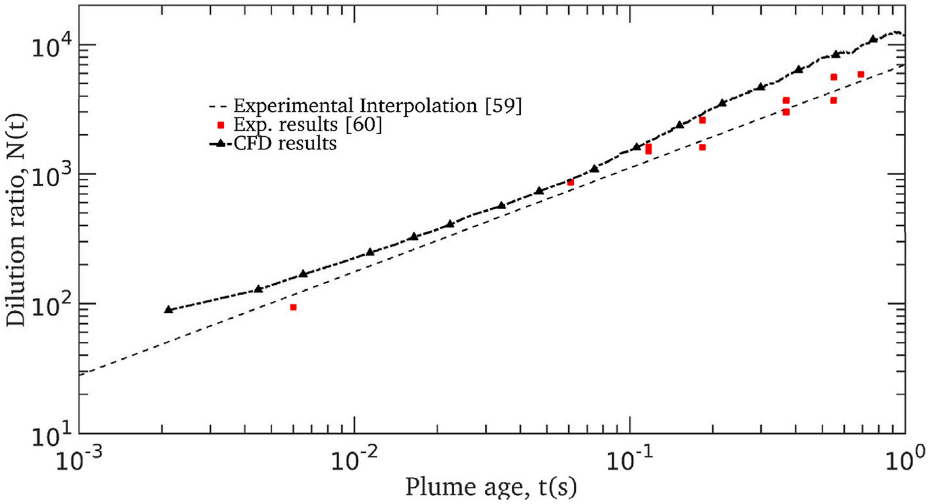

Fig. 3. Evolution of the predicted dilution ratio along the engine jet centerline against in-flight interpolated measurements (Schumann et al., 1998) and in-situ measurements (Schumann et al., 1996).

of 100 %, two different FSC (700 and 20 ppm) and three different emission soot number indices (EI_n, 1.38×10^{13}, 1.38×10^{14}, and 1.38×10^{15} #/kg-fuel). A validation of the plume dilution is first presented, and then the effects of FSC, ambient temperature and soot number EI_n on the evolution of ice crystals microphysical properties are presented in the following sections.

5.1. Validation of the jet plume dilution

One way to evaluate the dispersion of gaseous pollutants and particles emitted by a turbofan into the atmosphere is to compare their dilution with the interpolation of experimental data established by Schumann (Schumann et al., 1998). Since the contrail diameter can be represented by the expansion of passive particles in the jet, this allows for an appropriate assessment of the jet mixing process with ambient air. The dilution ratio N_D based on the contrail diameter is calculated as follows:

$$N_D = \frac{A\rho V}{\dot{m}_{fuel}} \tag{9}$$

with A representing the plume cross-sectional area, ρ the air density within the exhaust plume, V the velocity of the aircraft, and $\dot{m}_{fuel}$ the fuel flow rate. Fig. 3 shows the evolution of the dilution ratio $N(t)$ in comparison with the bulk mean dilution interpolated from in-flight measurements (Schumann et al., 1998) and with in-situ measurements of (Schumann et al., 1996). The interpolation was based on a large dataset from more than 70 plume encounters with the DLR Falcon research aircraft and the NASA ER-2 aircraft. As the emitted particles expand radially in the atmosphere with the plume age, the plume cross-sectional area A increases, leading to an increase in N_D. A very good agreement was observed up to 10^{-1} s, and a slight overprediction of the computed dilution ratio was observed beyond 3×10^{-1} s in the plume age.

5.2. Effects of fuel sulfur content on near-field contrail formation

5.2.1. Evolution on the plume chemistry

Sulfur species play a crucial role in the activation of soot particles as well as in the formation and growth of volatile particles, whereas water vapor primarily contributes to the growth of water droplets and ice crystals. Fig. 4 illustrates the evolution of the molar fractions of H_2O (Fig. 4-a), H_2SO_4 (Fig. 4-b) and SO_3 (Fig. 4-c) as functions of distance from the engine up to 120 m (approximately 0.5 s). These evolutions are presented for four different scenarios: with and without microphysics coupling, and with two different FSC (700 and 20 ppm). First, we analyze the case for $T_a = 218.8$ K and FSC = 700 ppm. Starting from an initial value of $X_{H_2O} = 3 \times 10^{-2}$ near the engine exit (the maximum in the plume), X_{H_2O} decreases by approximately two orders of magnitude due to plume dilution over a distance of 120 m. However, it does not reach the ambient molar fraction value ($X_{H_2O} = 9.55 \times 10^{-5}$) The middle and right panels show the molar fractions of H_2SO_4 and SO_3, respectively. Their molar fractions peak near the engine exit, and then decrease continuously due to plume dilution, with reductions of approximately two orders of magnitude for H_2SO_4 and four orders of magnitude for SO_3 at 120 m. This trend aligns well with numerical results from (Khou et al., 2016). The maximum concentration of SO_3 occurs closer to the engine than that of H_2SO_4, reflecting differences in their formation pathways (Khou et al., 2016). The subsequent decline in both species is primarily driven by dilution processes. When the FSC is reduced to 20 ppm, both $X_{H_2SO_4}$ and X_{SO_3} are shifted downward by approximately one and a half orders of magnitude. Interestingly, this reduction in FSC does not influence the molar fraction of water vapor, indicating its relative independence from sulfur content in the fuel in the near field. The impact of aerosol coupling is also analyzed. Beyond dilution, the coupling effects further reduce the molar fractions of H_2SO_4 and SO_3 due to processes such as activation and condensation on aerosol surfaces. In the high FSC case (700 ppm), coupling has a minimal impact on X_{H_2O} but causes a slight decrease in $X_{H_2SO_4}$ and X_{SO_3} around 40 m as compared to the uncoupled case due to activation and condensation processes. In the low FSC case (20 ppm), coupling does not significantly affect X_{SO_3}, but a modest decrease in of $X_{H_2SO_4}$ begins to appear

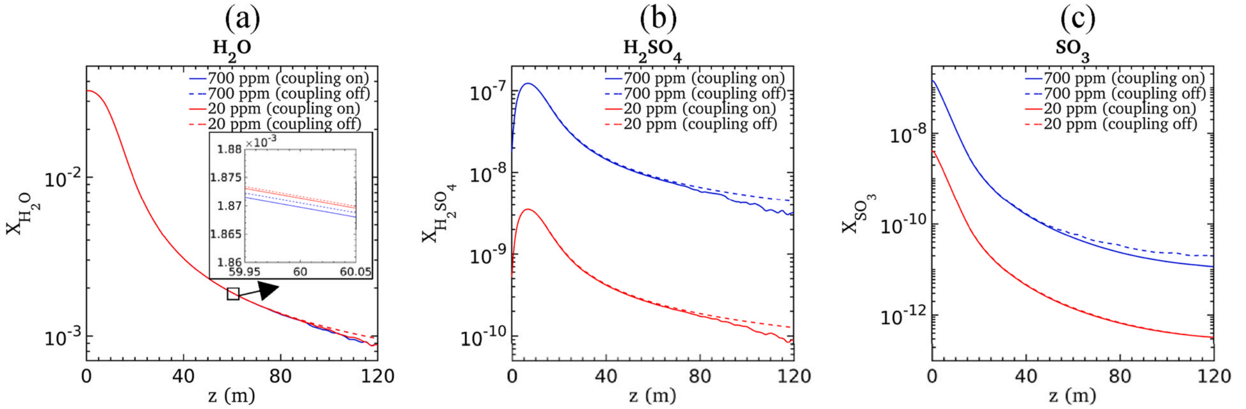

Fig. 4. Evolution of (a) H_2O, (b) H_2SO_4, and (c) SO_3 molar fraction in the plume centerline for FSC = 700 ppm and 20 ppm at 218.8 K.

at around 40 m. Growth of droplets and ice crystals by condensation of water vapor and ice deposition, respectively, decrease X_{H_2O} by around 80 m for both FSC.

5.2.2. *Effect on the thermodynamical properties of soot particles*

Each particle is assumed to be in thermal equilibrium with the local gas; thus, the particle temperature equals the gas temperature at that location. The mean temperature of particles T_p^m shown in Fig. 5 is computed as a spatial average over all particles. As shown in Fig. 5, the mean temperature of particles T_p^m (on the right axis) varies between 550 and 490 K, depending on the ambient temperature T_a. The temperature T_p^m drops rapidly after emission as a result of mixing with cold ambient air, approaching the ambient level at a plume age of $\sim$ 0.4 s ($z = 100$–110 m), when the jet plume is diluted by a factor of around 8000 (see Fig. 3). The mean saturation of water of particles S_w^m (on the left axis) for FSC = 700 ppm increases before reaching the equilibrium state ($S_w^m = 1$) around 30 m and 55 m for 212 and 218.8 K, respectively, whereas the equilibrium state in the jet plume is never reached on average for the four temperatures. The peak mean of S_w^m increases with decreasing T_a (reaching values of around 2.7 and 0.7 for 212 and 225 K, respectively). The large increase of S_w^m at 212 K is due to the non-linearity between the saturation vapor pressure and temperature, as noted by (Bier et al., 2021). Also, the mean of S_w^m increases with decreasing FSC to 20 ppm. The increase is stronger with decreasing T_a.

5.2.3. *Effect on microphysical properties of particles*

Fig. 6 compares the spatial distributions of plume particles in terms of the effects of the ambient temperature (Fig. 6-a) and FSC (Fig. 6-b), up to 180 m behind the engine. In Fig. 6-a, the effect of ambient temperatures 212 and 218.8 K were investigated at FSC of 700 ppm. At $T_a = 218.8$ K, soot particles remain unfrozen within the first 10 m of the plume, while freezing occurs near the plume edge in colder surroundings. For $T_a = 212$ K, plume cooling progresses faster at the edge, leading to water saturation and droplet formation earlier (10 m) than at the center (55 m). Ice crystals form between the edge and center around 20 m and spread toward the core by 75 m. In the $T_a = 218.8$ K case, droplet formation occurs later (80 m), and ice crystal growth is weaker as compared to the colder scenario. This could be attributed to the higher water saturation in the plume for the colder case, as shown in Fig. 5, which determines the ice crystals formation (Paoli et al., 2013). Fig. 6-b compares the spatial distributions of plume soot particles for FSC of 700 ppm and 20 ppm at 218.8 K. For both cases, the onset of ice crystals formation appears on the edge of the jet at the same distance behind the engine, i.e., x ~20 m.

Fig. 7 presents the effects of ambient temperature and FSC on the microphysical properties of soot particles in an aircraft engine plume. Fig. 7-a shows that the evolution of the mean radius of frozen soot particles increases significantly as the ambient temperature decreases, highlighting the stronger condensation and deposition processes under colder conditions. For 700 ppm, reducing the ambient temperature from 218.8 to 212 K increases the mean radius of ice-soot particles from 550 nm to 680 nm at 250 m, while at 223 K, no ice-soot particles are observed, indicating insufficient supersaturation to trigger ice crystal formation. Lowering the FSC to 20 ppm at 212 and 218.8 K slightly reduces the mean radius by approximately 50 nm at 250 m, consistent with previous studies showing that a higher FSC enhances ice crystal growth (Kärcher, 1998; Khou et al., 2016). The evolution of the activation Φ_{act} and freezing Φ_{frz} fractions in Fig. 7-b shows that all soot particles are activated and frozen at 100 m for 212 K, whereas at 218.8 K, only 70 % of the soot particles are frozen at 150 m for 700 ppm. Reducing the FSC to 20 ppm enhances the freezing fraction at 218.8 K to 90 % around 130 m. These trends demonstrate that colder temperatures and lower FSC accelerate ice crystal formation by promoting faster activation and freezing of soot particles. Similar findings by (Wong & Miake-Lye, 2010) found that a higher number of ice crystals formed from soot particles at a lower sulfur content. In the low sulfur scenario, binary homogeneous nucleation does not significantly deplete the gas phase. As a result, water depletion remains less effective due to the reduced availability of SO_3 and H_2SO_4. This leads to

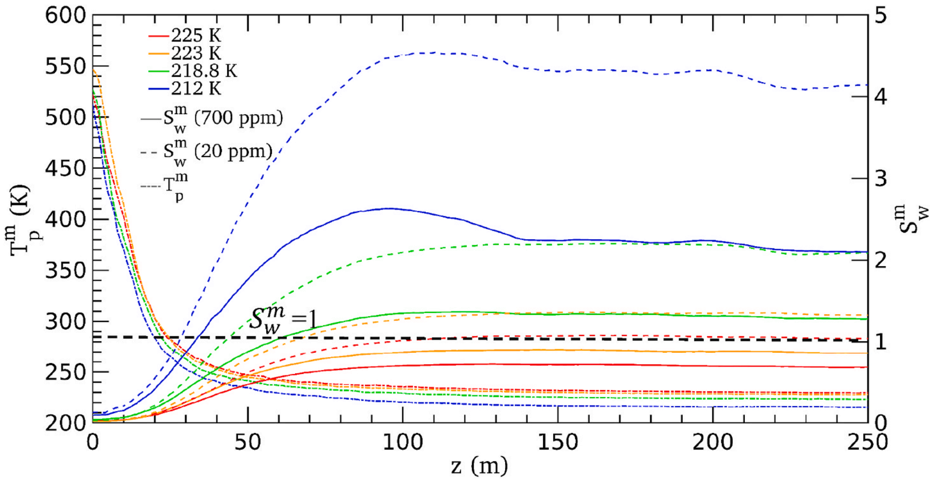

Fig. 5. Evolution of the mean temperature (left axis) and water saturation ratio (right axis) on computed particles for FSC = 700 ppm and 20 ppm at four ambient temperatures.

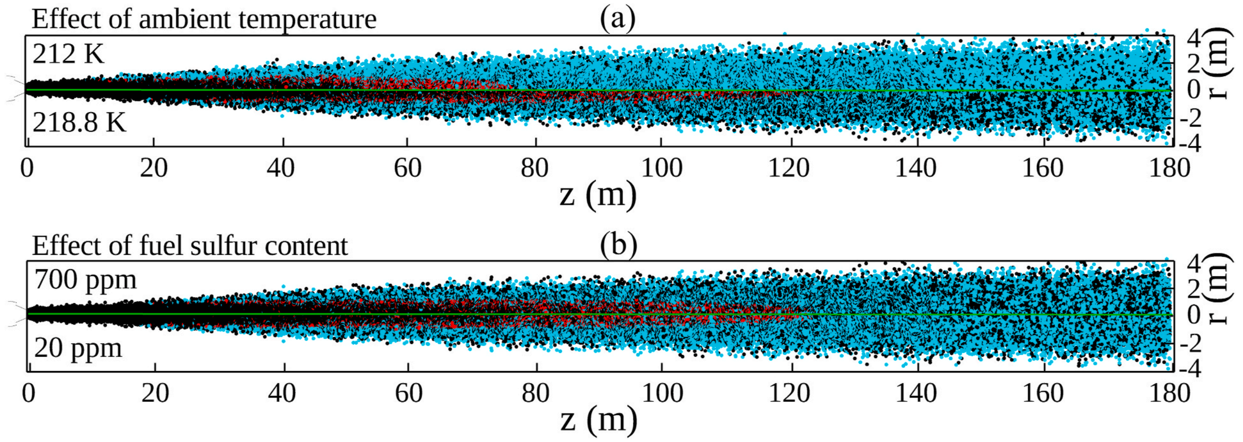

Fig. 6. Comparison of the spatial distribution of soot particles, being dried (black), activated (red points) and frozen (cyan points), (a) for ambient temperature at 212 K and 218.8 K at 700 ppm, and (b) for 700 ppm and 20 ppm at 218.8 K. (For interpretation of the references to colour in this figure legend, the reader is referred to the Web version of this article.)

a higher concentration of water vapor, which increases water supersaturation, as illustrated in Fig. 5. Consequently, higher water saturation in the plume enhances the formation of ice crystals, which plays a dominant role in the overall ice crystal formation process, as previously observed by (Paoli et al., 2013). The increased water supersaturation in the plume reduces the activation diameter of soot particles, resulting in a higher fraction of ice crystals originating from soot particles, as demonstrated by (Yu and Kärcher and Anderson, 2024). At 223 K, both fractions remain at zero, confirming that the temperature is too high for ice formation. The mean condensed mass evolution of water and ice on soot particles, shown in Fig. 7-c, further supports these observations. At 212 K, water quickly condenses and freezes, leading to a rapid conversion to ice within 100 m. At 218.8 K, water persists over a longer distance (∼130 m), indicating slower condensation and freezing. A higher FSC (700 ppm) enhances both water and ice masses on soot particles at a given temperature, reflecting greater water activation and ice deposition. Conversely, at 223 K, no significant mass of water or ice is observed on soot particles, consistent with the absence of ice crystal formation in Fig. 7-a and Fig. 7-b. Finally, Fig. 7-d presents the probability density function (PDF) ice particles based on frozen soot particle radii at 150 m behind the engine. The distribution shifts toward larger particle sizes as the temperature decreases, indicating more significant ice growth at colder temperatures. For a fixed temperature, a higher FSC results in larger ice crystals, consistent with the greater water and ice masses observed in Fig. 7-c and the increased mean radius in Fig. 7-a. These results demonstrated the critical interplay between temperature and FSC in shaping the size and growth of ice crystals in the plume. Overall, the analysis highlighted that colder ambient temperatures and higher FSC promote faster and more efficient ice deposition, resulting in larger ice crystals based on soot particles, while lower FSC increase the number of ice crystals formed from soot particles.

Fig. 8 presents the evolution of mean aqueous and non-aqueous surface coverage fractions (Θ_{aq} and Θ_{non-aq}) (Fig. 8-a and -b), as well as the mean condensed masses of sulfuric acid (m_{sulf}) and organic compounds (m_{org}) (Fig. 8-c and -d). These results are provided for three ambient temperatures (212, 218.8, and 223 K) and two FSC (700 and 20 ppm). In Fig. 8-a, the aqueous fraction Θ_{aq} increases rapidly at the beginning of the plume for both sulfur levels. For 700 ppm, Θ_{aq} reaches a maximum of approximately 0.73 at all three ambient temperatures, reflecting significant adsorption of water-soluble compounds. Lower temperatures lead to faster growth rates, with Θ_{aq} reaching a plateau sooner. The non-aqueous fraction Θ_{non-aq} representing water-insoluble organics grew until reaching a plateau value of $\Theta_{non-aq} = 0.27$ lower as compared to Θ_{aq}. This highlighted the dominance of aqueous over non-aqueous compounds under high sulfur conditions. For 20 ppm, Θ_{aq} and Θ_{non-aq} increase to 0.6 and 0.3, respectively. These results highlight the dominance of aqueous over non-aqueous compounds under both sulfur conditions. In Fig. 8-b, the ratio ($\Theta_{aq}/\Theta_{non-aq}$) underscores the dominance of aqueous components over non-aqueous ones, particularly at higher sulfur contents. For 700 ppm, the ratio reaches a peak of ∼2.7 at 100 m, indicating a strong preference for aqueous compound condensation. Lowering FSC to 20 ppm decreases the ratio ($\Theta_{aq}/\Theta_{non-aq}$) to ∼ 2. Fig. 8-c presents the mass evolutions of sulfuric acid m_{sulf} and organic compounds m_{org} on the surface of soot particles. At higher FSC and lower temperatures, the organic mass m_{org} increases more rapidly and dominates early in the plume, particularly at 212 K. This result indicates that increasing FSC enhanced the organic mass on soot particles. In contrast, the increase in sulfuric acid mass with higher FSC and lower ambient temperatures is less pronounced. Both masses m_{sulf} and m_{org} decrease under lower FSC and warmer conditions, reflecting reduced growth by condensation of sulfuric acid and organic species. In Fig. 8-d, the ratio $m_{org}/\ m_{sulf}$ provides insights into the relative contributions of organic compounds and sulfuric acid to the particle surface. At 700 ppm, the ratio decreases sharply in the near-field region (up to ∼ 50 m) to values around 1, indicating that m_{sulf} is nearly equal to m_{org}. This ratio subsequently increases significantly to ∼1000 by 250 m, showing a transition where organic compounds become more influential. For 218.8 K and 700 ppm, the ratio follows a similar trend but stabilizes at a lower value (∼100). At 223 K, the increase is more gradual, reaching a final value of ∼4, which reflects a balance between organics and sulfuric acid. In contrast, at 20 ppm, the ratio is consistently higher across the plume. It peaks at ∼400 in the near field and declines gradually toward a final value between ∼20 and ∼60 by 250 m as the

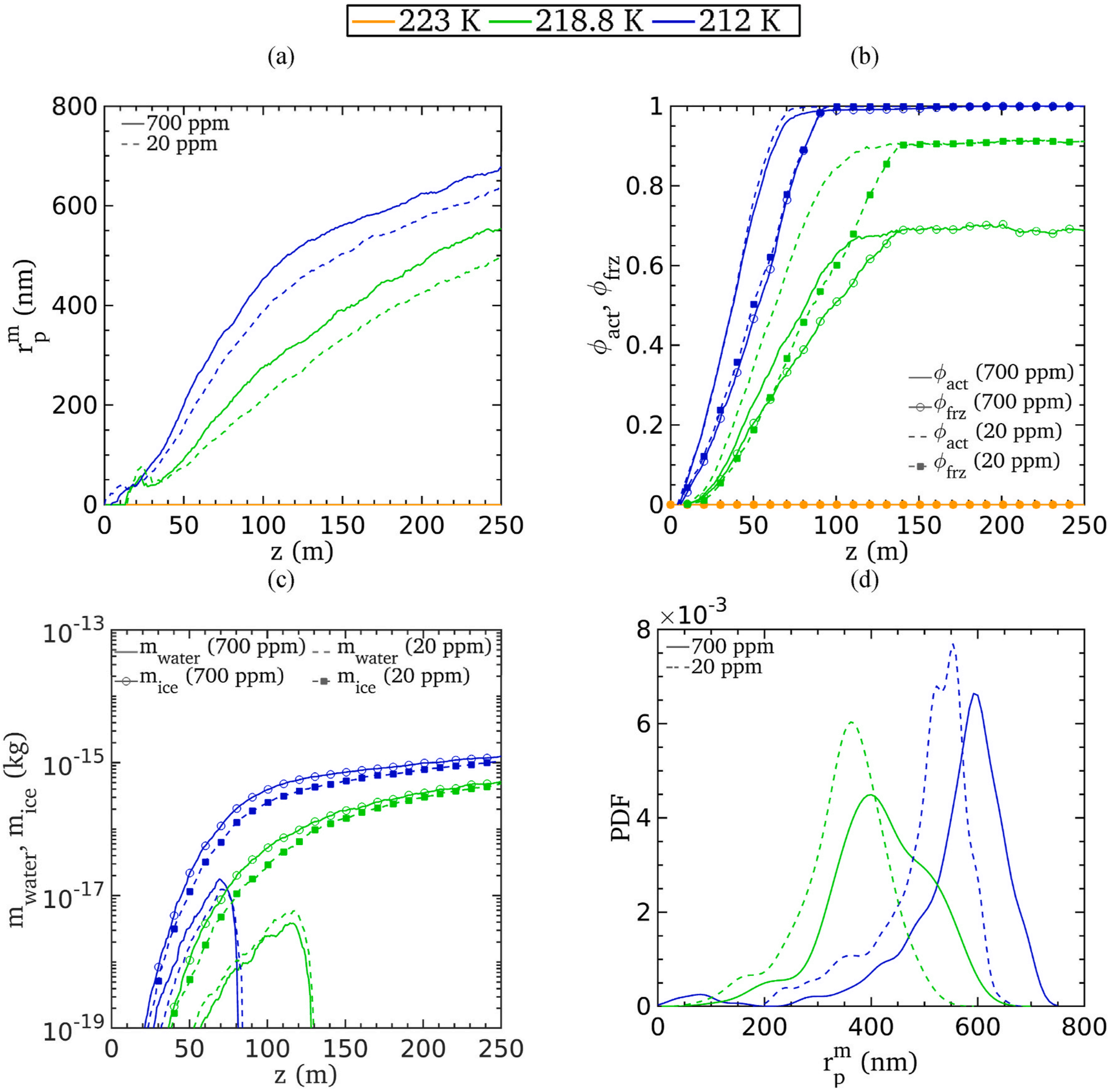

Fig. 7. Spatial evolution of: (a) mean radius of frozen soot particles, (b) the fraction of soot particles activating into water droplets and forming ice crystals, (c) the mean condensed mass of water and ice on soot particles, and (d) the probability density function (PDF) of the frozen soot particle radius at 150 m behind the engine. Results are shown for FSC = 700 and 20 ppm at different ambient temperatures: 223K, 218.8K, and 223K.

temperature decreases. This suggests an increasing predominance of organic compounds on soot particles for both FSC. These results highlight the competition between sulfuric acid and organics in plume microphysics under varying ambient temperature and FSC conditions. They confirm that FSC does modify ice crystal sizes in the near field, as well as the mass transfer rate, since this scales with the activated surface, as found by previous studies (Kärcher, 1998; Khou et al., 2016).

Fig. 9 shows the effect of ambient temperature (top panels) and sulfur content (bottom panels) on the predicted chemical composition of soot particles in the plume. As soot particles are hydrophobic at the nozzle exit, water condensation on their surface is initially limited. In the top panels, comparing 212 and 223 K, the higher ambient temperature leads to a significant presence of sulfuric acid and organics on the soot particles' surface over the plume length, where sulfuric acid is the dominant component in term of mass. Water vapor condensation is inhibited due to the relatively high ambient temperature. Conversely, at 212 K, the chemical composition is dominated by ice and water at the soot surface, which quickly becomes the prevailing component. This early water presence near the nozzle is driven by rapid activation by sulfuric acid and water-soluble organic compounds, combined with the low plume temperature under cold atmospheric conditions (212 K). Soot particles become predominantly covered with ice after approximately 10 m. This highlights how colder ambient temperatures favor the condensation of water and ice on soot particles. In the bottom panels, the influence of the sulfur content is evident. At 700 ppm, carbonyls and sulfuric acid contribute prominently to the soot particles' surface composition throughout the plume, particularly in the near field ($z < 15$ m). However, at 20 ppm, the lower sulfur content leads to a reduced contribution of sulfuric acid to below 1 % of the total mass, and the soot particle composition becomes dominated by organics

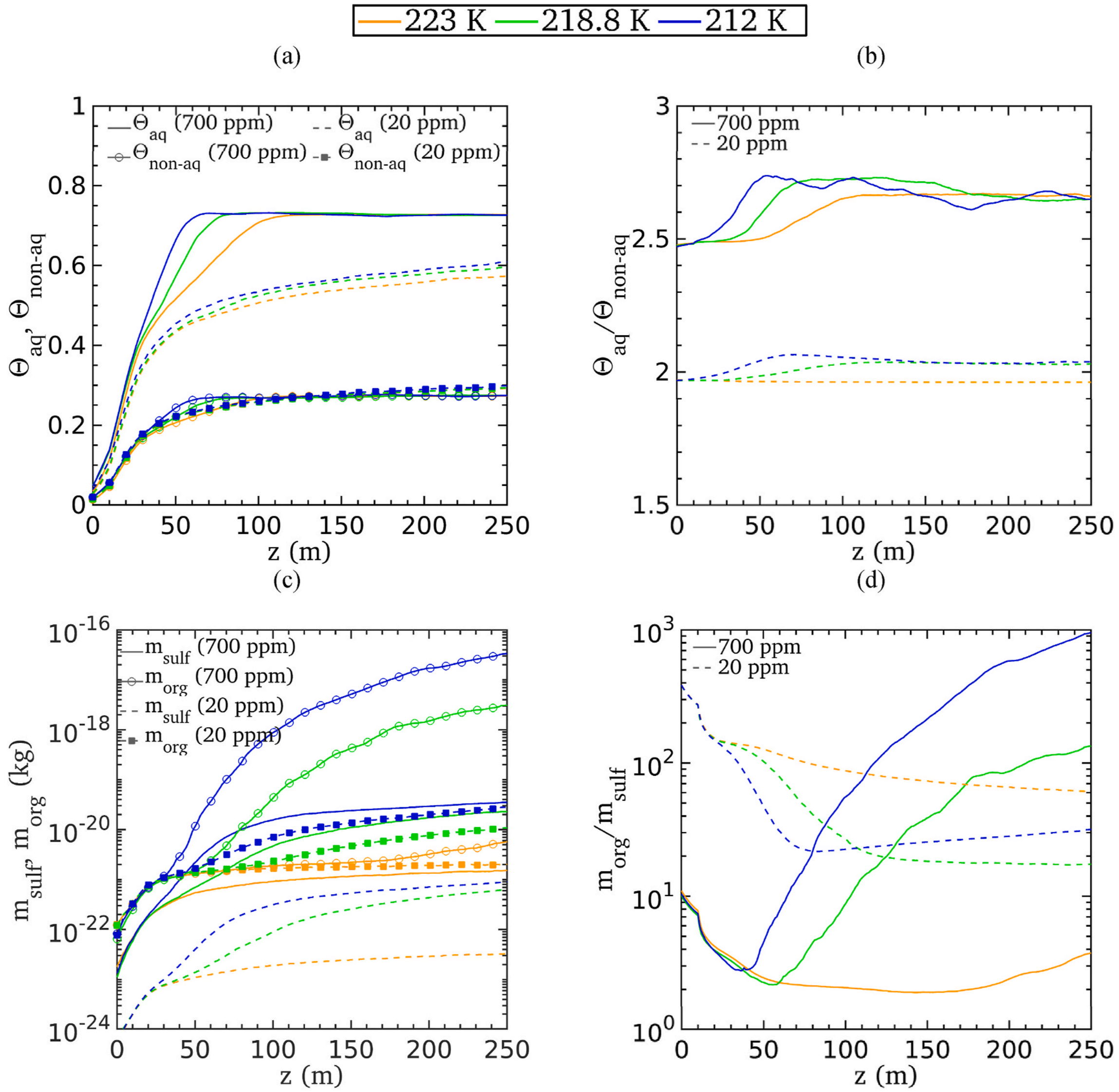

Fig. 8. Spatial evolution of: (a) the mean aqueous/non-aqueous soot particles surface, (b) the ratio of the mean aqueous/non-aqueous soot particles surface, (c) the mean condensed mass of sulfuric acid and organic compound on soot particles, and (d) the ratio of the mean condensed mass of sulfuric acid and organic compound on soot particles. Results are shown for FSC = 700 and 20 ppm at different ambient temperatures: 223K, 218.8K, and 223K.

up to approximately 15 m. This result highlights the significant mass contribution of organic compounds compared to sulfuric acid, regardless of the FSC.

Fig. 10 presents the particle size distributions at a distance of 120 m (approximately 0.5 s after exhaust) for different particle classes, highlighting the effects of the FSC in the left panel (Fig. 10-a) and ambient temperature in the right panel (Fig. 10-b). In the left panel, the effect of the sulfur content is presented for a temperature of 218.8 K. At 700 ppm, a higher sulfuric acid availability promotes the nucleation of ultrafine volatile particles ($D_p < 10$ nm), as seen from the higher concentration of hydrates and volatile particles, around 10^{13} #/cm^3 at $D_p \approx 0.6$ nm. At 20 ppm, the lower sulfur content reduces the concentration of hydrates and volatile particles around 10^9 #/cm^3. All soot particles are either activated as droplets or transformed into ice crystals. Furthermore, the reduction in sulfur content appears to produce slightly smaller activated soot droplets and soot-derived ice crystals, which dominate the larger particle range $D_p > 100$ nm. The concentration of soot as droplets or ice crystals increases slightly with decreasing FSC. For the effect of temperature (Fig. 10-b, right panel), increasing the temperature from 212 to 223 K significantly impacts the particle distributions. The peak concentration of hydrates decreases from 2×10^{13} #/cm^3 at 212 K to approximately 10^{13} #/cm^3 at 223 K. However, the average diameter of the hydrates increases slightly, with particles at 223 K exhibiting a mean diameter 0.1 nm larger than at 212 K. At 212 K, all soot particles are converted into ice crystals, forming the largest particle sizes among all temperatures, with a mean diameter of approximately 1 μm. At the intermediate temperature of 218.8 K, both activated soot droplets and soot-derived ice crystals are

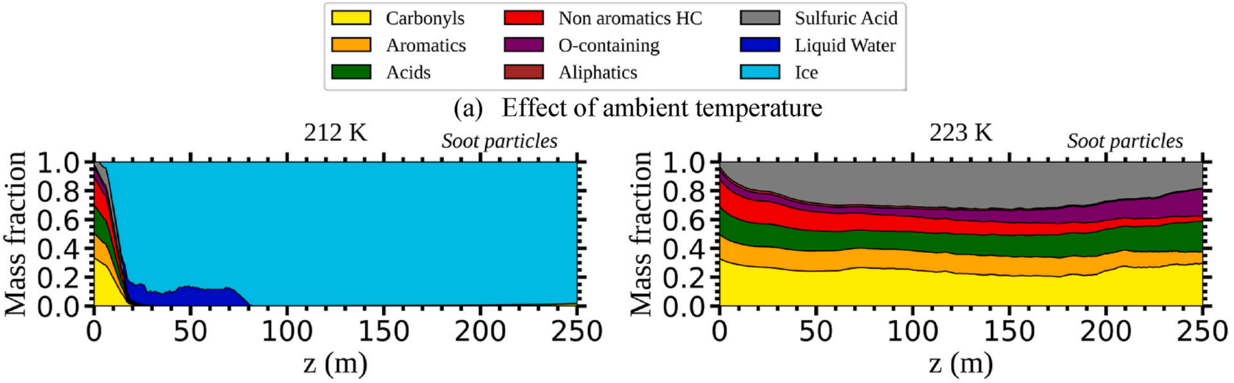

(a) Effect of ambient temperature

(b) Effect of fuel sulfur content

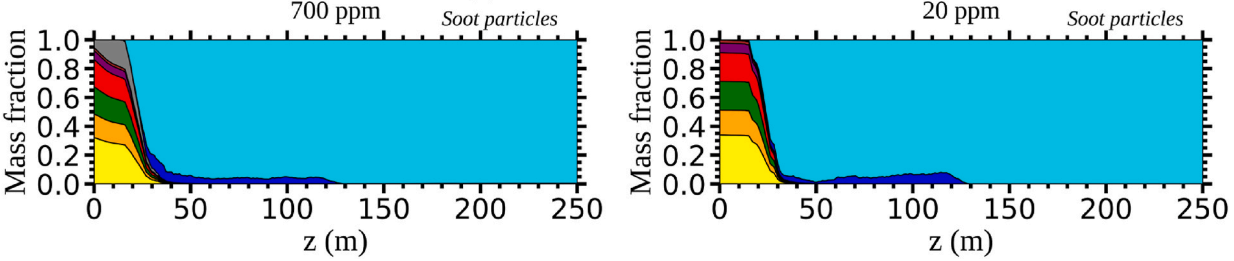

Fig. 9. Effect of (a) ambient temperature on the soot particles' chemical composition for 212 and 218.8 K at 700 ppm, and effect of (b) FSC on the soot particles' chemical composition for 700 and 200 ppm at 218.8 K.

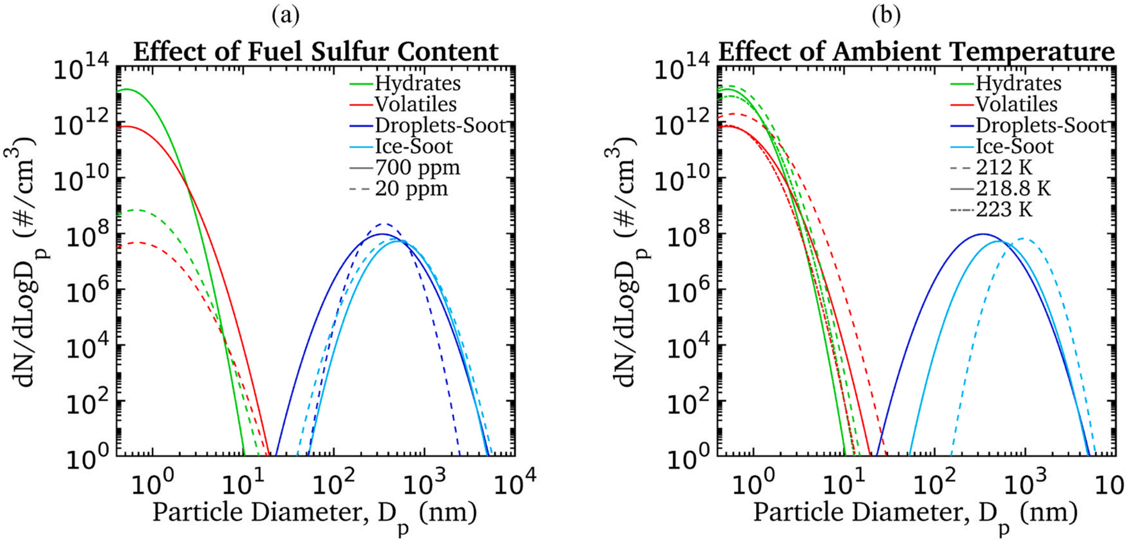
(a) (b)

Fig. 10. Particle size distributions regarding the (a) effect of FSC and (b) effect of ambient temperature at 120 m.

observed. The concentration of ice crystals at this temperature is comparable to that at 212 K (10^8 #/cm^3), but their mean diameter is significantly smaller, around 400 nm. At 223 K, no activated soot droplets or soot-derived ice crystals are reported in the results, indicating that higher temperatures inhibit the freezing and activation processes for soot particles.

5.3. Effect of emission index of soot particles on near-field contrail formation

In this section, two additional emission indices of soot number $EI_N = 1.38 \times 10^{13}$ and 1.38×10^{15} #/kg-fuel for the soot-poor regime and the soot-rich regime (Karcher & Yu, 2009), were chosen respectively to investigate ice crystals formed from emitted soot particles ("Ice-Soot") at 250 m (approximately 1 s) behind the engine for 218.8 K for three soot emission indices ($EI_N = 1.38 \times 10^{13}$, 1.38×10^{14}, and 1.38×10^{15} #/kg-fuel) and two FSC

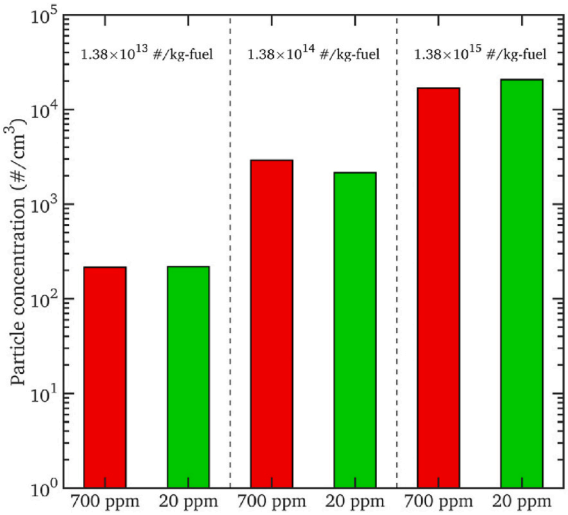

Fig. 11. Comparison of ice-soot particle concentration for different soot emission indices at 218.8 K. Red bars indicate a FSC of 700 ppm, while green bars indicate a FSC of 20 ppm. (For interpretation of the references to colour in this figure legend, the reader is referred to the Web version of this article.)

levels (700 and 20 ppm). For comparison at 1 s, ice-soot concentration falls within the expected range of 2×10^4–10^5 $\#/\mathrm{cm}^3$ for $EI_N \approx 10^{15}$ #/kg-fuel, as reported by other authors (Yu and Kärcher and Anderson, 2024; Karcher & Yu, 2009). While the FSC has a minimal impact on the concentration of ice-soot particles for $EI_N = 1.38 \times 10^{13}$, it slightly increases the ice-soot particles concentration with decreasing FSC.

Fig. 12 shows the particle size distributions as a function of particle diameter D_p for different soot emission indices at 120 m. For hydrates, there is no noticeable effect on the size distribution for $EI_N \leq 1.38 \times 10^{14}$ #/kg-fuel. However, at 1.38×10^{15} #/kg-fuel, the peak concentration decreases from 2×10^{13} $\#/\mathrm{cm}^3$ to approximately 5×10^{12} $\#\mathrm{cm}^3$, reflecting a reduced number of smaller particles. Larger volatile particles are formed for $EI_N \leq 1.38 \times 10^{14}$ #/kg-fuel. Regarding soot-derived ice crystals, EI_N strongly affects the peak concentration of ice crystals. The number concentration increased from 5×10^6 $\#/\mathrm{cm}^3$ at the lowest EI_N to 10^9 $\#/\mathrm{cm}^3$ at the highest EI_N. However, the average diameter decreased slightly as EI_N increased, likely due to competition for available moisture during freezing. For $EI_N = 1.38 \times 10^{13}$ #/kg-fuel, the size distribution of soot-derived ice crystals is broader, with mean diameters reaching approximately 600 nm due to broader size distributions, producing the largest ice particles, which reflects enhanced growth dynamics at this intermediate soot emission index.

6. Summary and conclusions

This work presents a CFD-microphysics coupling approach for accurately predicting the evolution and formation of ice crystals formed from soot particles in the near field of a turbofan engine. The approach employs a Eulerian–Lagrangian online coupling, based on a 2.5D axisymmetric Computational Fluid Dynamics (CFD) framework for engine plume dynamics, coupled with a gas-phase chemistry and a detailed microphysical model. This model considers intricate multicomponent interactions involving organic vapors, sulfur species, and soot particles emitted by the aircraft. An analysis was carried out for different ambient temperature, different FSC, and for different soot particle numbers.

The results demonstrated that colder ambient temperatures significantly enhance condensation and freezing processes, leading to higher ice crystal concentrations and larger mean sizes for soot-ice particles. At 212 K, the mean radius of soot-derived ice crystals reached approximately 680 nm, compared to 550 nm at 218.8 K, highlighting the influence of lower temperatures on ice particle growth. At low temperatures, ice crystal formation is more efficient due to higher water supersaturation, resulting in faster activation and freezing of soot particles. Additionally, decreasing the ambient temperature increases the mass of condensed organics on soot particles, with a stronger contribution from water-soluble organic species, further contributing to particle growth and the ice formation process. For hydrate particles, colder temperatures also promote homogeneous binary nucleation, resulting in a significant shift in the distribution of hydrate particles toward higher concentrations and larger sizes. Conversely, at warmer conditions near the threshold for contrail formation, ice crystal production is limited, with no soot-derived ice observed at the highest temperature studied. Under these warmer conditions, organic compounds dominate the particle surface composition.

The FSC strongly influences the freezing behavior and chemical composition of particles in the plume. At lower FSC (20 ppm), liquid water supersaturation is higher, reducing the activation diameter for soot particles and allowing a greater fraction to activate and freeze. At 218.8 K, the freezing fraction of soot particles reaches approximately 90 % at 20 ppm FSC, compared to 70 % at 700 ppm FSC. Although the model predicts a higher freezing fraction of soot particles under low FSC conditions, direct validation remains difficult. Existing experimental datasets, such as Petzold et al. (1997), suggest that early contrail formation is dominated by soot

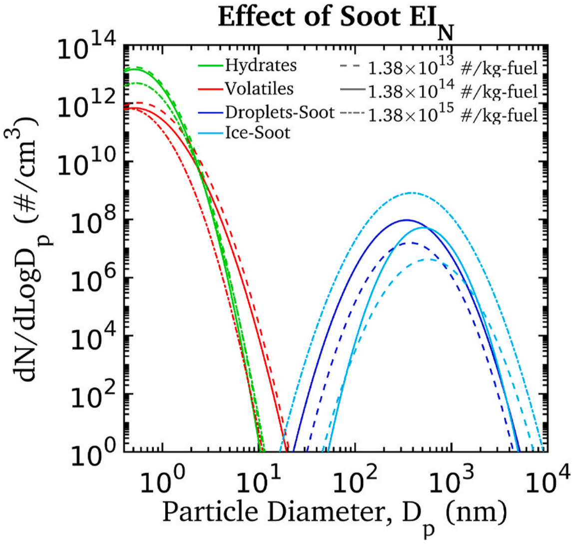

Fig. 12. Particle size distribution regarding the effect of the emission index of soot particles at 120 m.

activation, but their measurements reveal mixed trends and strong spatial variability. This highlights the need for more targeted in situ observations capable of isolating the contribution of soot particles as Ice Nuclei (IN) under varying FSC conditions in the near field. At lower FSC, the reduced availability of sulfuric acid shifts the condensation process toward organic compounds, increasing the contribution of organics to overall particle activation and growth. By contrast, a higher FSC (700 ppm) increases the fraction of water-soluble compounds on soot particle surfaces, enhancing water condensation and deposition. This promotes the growth of larger ice crystals while limiting the total number of ice particles due to reduced water supersaturation. Hydrates and volatile particles exhibit peak concentrations near 10^{13} #/cm^3 under high FSC, as compared to approximately 10^{11} #/cm^3 at low FSC, driven by increased sulfuric acid availability.

The soot emission index played a critical role in determining the number and size of soot-derived ice crystals. Higher emission indices increased ice crystal concentrations, while the lowest emission indices ($EI_N = 1.38 \times 10^{13}$ #/kg-fuel) produced the largest soot-derived ice particles, with mean diameters reaching approximately 600 nm due to broader size distributions and reduced competition for available moisture. Hydrates and volatile particles experienced reduced concentrations and sizes at higher soot emission indices, reflecting competition for moisture in soot-rich conditions.

Overall, this study highlights the interplay between temperature, fuel composition, and soot emissions in determining contrail properties. Colder temperatures and higher FSC enhance ice deposition efficiency, resulting in larger ice crystals, while lower FSC and higher soot emission indices promote the formation of more numerous ice crystals. The findings underline the critical role of organic compounds, particularly in low FSC conditions, in shaping particle growth and surface properties, and thereby influencing the ice formation dynamics. The inclusion of detailed microphysics and chemical processes in the model provides a comprehensive understanding of contrail formation dynamics, offering valuable insights for improving contrail prediction and mitigating the climate impact of aviation. Future work will be focused on evaluating the effects of alternative fuels on contrail formation.

CRediT authorship contribution statement

S. Cantin: Writing – review & editing, Writing – original draft, Visualization, Validation, Software, Methodology, Investigation, Formal analysis, Data curation, Conceptualization. **M. Chouak:** Writing – review & editing, Supervision, Conceptualization. **F. Garnier:** Writing – review & editing, Supervision, Resources, Project administration, Funding acquisition, Conceptualization.

Declaration of competing interest

The authors declare the following financial interests/personal relationships which may be considered as potential competing interests: Francois Garnier reports financial support was provided by Safran Aircraft Engines. If there are other authors, they declare that they have no known competing financial interests or personal relationships that could have appeared to influence the work reported in this paper.

Acknowledgment

This study was supported by Safran Aircraft Engines (SAE). CFD computations were carried out on the Narval supercomputer at École de technologie supérieure. This research was enabled in part by support provided by Calcul Québec (calculquebec.ca) and the

Digital Research Alliance of Canada (alliancecan.ca).

Data availability

Data will be made available on request.

References

Ahrens, D., Méry, Y., Guénard, A., & Miake-Lye, R. C. (2022). A new approach to estimate particulate matter emissions from ground certification data: The nvPM mission emissions estimation methodology. *ASME Journal of Engineering for Gas Turbine and Power, 3*(145). https://doi.org/10.1115/1.4055477, 031019-031019-031012.

Airbus. (2023). *Global market forecast 2023–2042*. https://www.airbus.com/en/products-services/commercial-aircraft/global-market-forecast Accessed 16 January 2025.

Bier, A., Unterstrasser, S., & Vancassel, X. (2021). Box model trajectory studies of contrail formation using a particle-based cloud microphysics scheme. *Atmospheric Chemistry and Physics, 2*(22), 823–845. https://doi.org/10.5194/acp-2021-361

Bier, A., Unterstrasser, S., Zink, J., Hillenbrand, D., Jurkat-Witschas, T., & Lottermoser, A. (2023). Contrail formation on ambient aerosol particles for aircraft with hydrogen combustion: A box model trajectory study. *Atmospheric Chemistry and Physics, 4*(24), 2319–2344. https://doi.org/10.5194/acp-24-2319-2024

Brown, R. C., Miake-Lye, R. C., Anderson, M. R., & Kolb, C. E. (1996). Aerosol dynamics in near-field aircraft plumes. *Journal of Geophysical Research: Atmospheres, D17* (101), 22939–22953. https://doi.org/10.1029/96JD01918

Cantin, S., Chouak, M., & Garnier, F. (2024). Eulerian-Lagrangian CFD-microphysics modeling of aircraft-emitted aerosol formation at ground-level. *Aerospace Science and Technology, 12*(58), 1347–1370. https://doi.org/10.1080/02786826.2024.2395940

Cantin, S., Chouak, M., Morency, F., & Garnier, F. (2021). Eulerian–Lagrangian CFD-microphysics modeling of a near-field contrail from a realistic turbofan. *International Journal of Engine Research, 4*(23), 661–677. https://doi.org/10.1177/1468087421993961

Casati, R., Scheer, V., Vogt, R., & Benter, T. (2007). Measurement of nucleation and soot mode particle emission from a diesel passenger car in real world and laboratory in situ dilution. *Atmospheric Environment, 10*(41), 2125–2135. https://doi.org/10.1016/j.atmosenv.2006.10.078

CD-Adapco. (2021). *STAR-CCM+ documentation version 16.06.008*.

Celik, I. B., Ghia, U., Roache, P. J., & Freitas, C. J. (2008). Procedure for estimation and reporting of uncertainty due to discretization in CFD applications. *ASME Journal of Fluids Engineering, 7*(130). https://doi.org/10.1115/1.2960953, 078001-078001-078004.

Fritz, T. M., Eastham, S. D., Speth, R. L., & Barrett, S. R. H. (2020). The role of plume-scale processes in long-term impacts of aircraft emissions. *Atmospheric Chemistry and Physics, 9*(20), 5697–5727. https://doi.org/10.5194/acp-20-5697-2020

Fuchs, N. A., & Sutugin, A. G. (1971). High-dispersed aerosols. In G. M. Hidy, & J. R. Brock (Eds.), *Topics in current aerosol research* (pp. 1–60). New York: Pergamon Press. https://doi.org/10.1016/B978-0-08-016674-2.50006-6.

Gao, K., & Kanji, Z. A. (2022). Impacts of simulated contrail processing and organic content change on the ice nucleation of soot particles. *Geophysical Research Letters, 16*(49), Article e2022GL099869. https://doi.org/10.1029/2022GL099869

Garmory, A., Britter, R. E., & Mastorakos, E. (2008). Simulation of the evolution of aircraft exhaust plumes including detailed chemistry and segregation. *Journal of Geophysical Research: Atmospheres, D8*(113). https://doi.org/10.1029/2007JD009104. n/a-n/a.

Garnier, F., Baudoin, C., Woods, P., & Louisnard, N. (1997). Engine emission alteration in the near field of an aircraft. *Atmospheric Environment, 12*(31), 1767–1781. https://doi.org/10.1016/S1352-2310(96)00329-9

Garnier, F., Maglaras, E., Morency, F., & Vancassel, X. (2014). Effect of compressibility on contrail ice particle growth in an engine jet. *International Journal of Turbo and Jet Engines, 2*(31), 131–140. https://doi.org/10.1515/tjj-2013-0039

Gorbunov, B., Baklanov, A., Kakutkina, N., Windsor, H. L., & Toumi, R. (2001). Ice nucleation on soot particles. *Journal of Aerosol Science, 2*(32), 199–215. https://doi.org/10.1016/S0021-8502(00)00077-X

Guignery, F., Montreuil, E., Thual, O., & Vancassel, X. (2012). Contrail microphysics in the near wake of a realistic wing through RANS simulations. *Aerospace Science and Technology, 1*(23), 399–408. https://doi.org/10.1016/j.ast.2011.09.011

Jacobson, M. Z. (2005). *Fundamentals of atmospheric modeling* (2nd ed.). Cambridge: Cambridge University Press. https://doi.org/10.1017/CBO9781139165389

Jathar, S. H., Miracolo, M. A., Presto, A. A., Donahue, N. M., Adams, P. J., & Robinson, A. L. (2012). Modeling the formation and properties of traditional and non-traditional secondary organic aerosol: Problem formulation and application to aircraft exhaust. *Atmospheric Chemistry and Physics, 19*(12), 9025–9040. https://doi.org/10.5194/acp-12-9025-2012

Kärcher, B. (1998). Physicochemistry of aircraft-generated liquid aerosols, soot, and ice particles: 1. Model description. *Journal of Geophysical Research: Atmospheres, D14*(103), 17111–17128. https://doi.org/10.1029/98JD01044

Kärcher, B. (2018). Formation and radiative forcing of contrail cirrus. *Nature Communications, 1*(9), 1824–1841. https://doi.org/10.1038/s41467-018-04068-0

Kärcher, B., Burkhardt, U., Bier, A., Bock, L., & Ford, I. J. (2015). The microphysical pathway to contrail formation. *Journal of Geophysical Research: Atmospheres, 15* (120), 7893–7927. https://doi.org/10.1002/2015JD023491

Kärcher, B., Hendricks, J., & Lohmann, U. (2006). Physically based parameterization of cirrus cloud formation for use in global atmospheric models. *Journal of Geophysical Research: Atmospheres, D1*(111), 11. https://doi.org/10.1029/2005JD006219

Kärcher, B., Hirschberg, M. M., & Fabian, P. (1996). Small-scale chemical evolution of aircraft exhaust species at cruising altitudes. *Journal of Geophysical Research: Atmospheres, D10*(101), 15169–15190. https://doi.org/10.1029/96JD01059

Kärcher, B., Möhler, O., DeMott, P. J., Pechtl, S., & Yu, F. (2007). Insights into the role of soot aerosols in cirrus cloud formation. *Atmospheric Chemistry and Physics, 16* (7), 4203–4227. https://doi.org/10.5194/acp-7-4203-2007

Kärcher, B., Peter, T., Biermann, U. M., & Schumann, U. (1996). The initial composition of jet condensation trails. *Journal of the Atmospheric Sciences, 21*(53), 3066–3083. https://doi.org/10.1175/1520-0469(1996)053<3066:ticojc>2.0.co;2

Kärcher, B., Turco, R. P., Yu, F., Danilin, M. Y., Weisenstein, D. K., Miake-Lye, R. C., & Busen, R. (2000). A unified model for ultrafine aircraft particle emissions. *Journal of Geophysical Research: Atmospheres, D24*(105), 29379–29386. https://doi.org/10.1029/2000jd900531

Karcher, B., & Yu, F. (2009). Role of aircraft soot emissions in contrail formation. *Geophysical Research Letters, 1*(36), L01804. https://doi.org/10.1029/2008GL036649

Khou, J. C. (2016). Modélisation des traînées de condensation par interaction entre l'aérodynamique, la cinétique chimique et la microphysique. Ph.D. Dissertation. *Ecole doctorale de Sciences mécaniques, acoustique, électronique et robotique de Paris*. Palaiseau, France: Université Pierre et Marie Curie. ONERA/EMI.

Khou, J. C., Ghedhaifi, W., Vancassel, X., Montreuil, E., & Garnier, F. (2016). CFD simulation of contrail formation in the near field of a commercial aircraft: Effect of fuel sulfur content. *Meteorologische Zeitschrift, 6*(26), 585–596. https://doi.org/10.1127/metz/2016/0761

Kılıç, D., Brem, B. T., Klein, F., El-Haddad, I., Durdina, L., Rindlisbacher, T., Setyan, A., Huang, R., Wang, J., Slowik, J. G., Baltensperger, U., & Prevot, A. S. H. (2017). Characterization of gas-phase organics using proton transfer reaction time-of-flight mass spectrometry: Aircraft turbine engines. *Environmental Science and Technology, 7*(51), 3621–3629. https://doi.org/10.1021/acs.est.6b04077

Kulmala, M. (1993). Condensational growth and evaporation in the transition regime. *Aerospace Science and Technology, 3*(19), 381–388. https://doi.org/10.1080/02786829308959645

Kurzke, J. (2004). *GasTurb 10: A program for gas-turbine performance calculations*. Germany: Dachau.

Lee, D. S., Fahey, D. W., Skowron, A., Allen, M. R., Burkhardt, U., Chen, Q., Doherty, S. J., Freeman, S., Forster, P. M., Fuglestvedt, J., Gettelman, A., De León, R. R., Lim, L. L., Lund, M. T., Millar, R. J., Owen, B., Penner, J. E., Pitari, G., Prather, M. J., Sausen, R., & Wilcox, L. J. (2020). The contribution of global aviation to anthropogenic climate forcing for 2000 to 2018. *Atmospheric Environment, 244*. https://doi.org/10.1016/j.atmosenv.2020.117834, 117834-117834-117829.

Lewellen, D. C. (2020). A large-eddy simulation study of contrail ice number formation. *Journal of the Atmospheric Sciences, 7*(77), 2585–2604. https://doi.org/10.1175/jas-d-19-0322.1

Li, W., Riemer, N., Xu, L., Wang, Y., Adachi, K., Shi, Z., Zhang, D., Zheng, Z., & Laskin, A. (2024). Microphysical properties of atmospheric soot and organic particles: Measurements, modeling, and impacts. *Npj Climate and Atmospheric Science, 1*(7), 65–79. https://doi.org/10.1038/s41612-024-00610-8

Lobo, P., Durdina, L., Smallwood, G. J., Rindlisbacher, T., Siegerist, F., Black, E. A., Yu, Z., Mensah, A. A., Hagen, D. E., Miake-Lye, R. C., Thomson, K. A., Brem, B. T., Corbin, J. C., Abegglen, M., Sierau, B., Whitefield, P. D., & Wang, J. (2015). Measurement of aircraft engine non-volatile PM emissions: Results of the aviation-particle regulatory instrumentation demonstration experiment (A-PRIDE) 4 campaign. *Aerospace Science and Technology, 7*(49), 472–484. https://doi.org/10.1080/02786826.2015.1047012

Määttänen, A., Merikanto, J., Henschel, H., Duplissy, J., Makkonen, R., Ortega, I. K., & Vehkamäki, H. (2018). New parameterizations for neutral and ion-induced sulfuric acid-water particle formation in nucleation and kinetic regimes. *Journal of Geophysical Research: Atmospheres, 2*(123), 1269–1296. https://doi.org/10.1002/2017JD027429

Mason, B. J. (1971). In C. Press (Ed.), *The physics of clouds* (2nd ed.). Oxford: Clarendon Press.

Mikhailov, E. F., Vlasenko, S. S., Krämer, L., & Niessner, R. (2001). Interaction of soot aerosol particles with water droplets: Influence of surface hydrophilicity. *Journal of Aerosol Science, 6*(32), 697–711. https://doi.org/10.1016/S0021-8502(00)00101-4

Paoli, R., Nybelen, L., Picot, J., & Cariolle, D. (2013). Effects of jet/vortex interaction on contrail formation in supersaturated conditions. *Physics of Fluids, 5*(25). https://doi.org/10.1063/1.4807063, 053305-053305-053327.

Petzold, A., Busen, R., Schröder, F. P., Baumann, R., Kuhn, M., Ström, J., Hagen, D. E., Whitefield, P. D., Baumgardner, D., Arnold, F., Borrmann, S., & Schumann, U. (1997). Near-field measurements on contrail properties from fuels with different sulfur content. *Journal of Geophysical Research: Atmospheres, D25*(102), 29867–29880. https://doi.org/10.1029/97JD02209

Ponsonby, J., King, L., Murray, B. J., & Stettler, M. E. J. (2023). Jet aircraft lubrication oil droplets as contrail ice-forming particles. *Atmospheric Chemistry and Physics, 3*(24), 2045–2058. https://doi.org/10.5194/acp-24-2045-2024

Presto, A. A., Hennigan, C. J., Nguyen, N. T., & Robinson, A. L. (2012). Determination of volatility distributions of primary organic aerosol emissions from internal combustion engines using thermal desorption gas chromatography mass spectrometry. *Aerospace Science and Technology, 10*(46), 1129–1139. https://doi.org/10.1080/02786826.2012.700430

Pruppacher, H. R., & Klett, J. D. (1998). Microphysics of clouds and precipitation. *Atmospheric Oceanographic Sciences Library, XXII*, 954. https://doi.org/10.1007/978-0-306-48100-0. Springer Netherlands. Dordrecht.

Rojo, C., Vancassel, X., Mirabel, P., Ponche, J.-L., & Garnier, F. (2014). Impact of alternative jet fuels on aircraft induced aerosols. *Fuel, 144*, 335–341. https://doi.org/10.1016/j.fuel.2014.12.021

Schröder, F., Brock, C. A., Baumann, R., Petzold, A., Busen, R., Schulte, P., & Fiebig, M. (2000). In situ studies on volatile jet exhaust particle emissions: Impact of fuel sulfur content and environmental conditions on nuclei mode aerosols. *Journal of Geophysical Research: Atmospheres, D15*(105), 19941–19954. https://doi.org/10.1029/2000JD900112

Schröder, F., Karcher, B., Duroure, C., Strom, J., Petzold, A., Gayet, J. F., Strauss, B., Wendling, P., & Borrmann, S. (2000). On the transition of contrails into cirrus clouds. *Journal of the Atmospheric Sciences, 4*(57), 464–480. https://doi.org/10.1175/1520-0469(2000)057<0464:OTTOCI>2.0.CO;2

Schumann, U., Schlager, H., Arnold, F., Baumann, R., Haschberger, P., & Klemm, O. (1998). Dilution of aircraft exhaust plumes at cruise altitudes. *Atmospheric Environment, 18*(32), 3097–3103. https://doi.org/10.1016/S1352-2310(97)00455-X

Schumann, U., Ström, J., Busen, R., Baumann, R., Gierens, K., Krautstrunk, M., Schröder, F. P., & Stingl, J. (1996). In situ observations of particles in jet aircraft exhausts and contrails for different sulfur-containing fuels. *Journal of Geophysical Research: Atmospheres, D3*(101), 6853–6869. https://doi.org/10.1029/95JD03405

Seinfeld, J. H., & Pandis, S. N. (2016). *Atmospheric chemistry and physics: From air pollution to climate change* (2nd ed.). Hoboken: John Wiley & Sons.

Slemr, F., Giehl, H., Habram, M., Slemr, J., Schlager, H., Schulte, P., Haschberger, P., Lindermeir, E., Döpelheuer, A., & Plohr, M. (2001). In-flight measurement of aircraft CO and nonmethane hydrocarbon emission indices. *Journal of Geophysical Research: Atmospheres, D7*(106), 7485–7494. https://doi.org/10.1029/2000JD900580

Timko, M. T., Herndon, S. C., Wood, E. C., Onasch, T. B., Northway, M. J., Jayne, J. T., Canagaratna, M. R., Miake-Lye, R. C., & Knighton, W. B. (2010). Gas turbine engine emissions—Part I: Volatile organic compounds and nitrogen oxides. *ASME Journal of Engineering for Gas Turbine and Power, 6*(132). https://doi.org/10.1115/1.4000131, 061504-061504-061514.

Timko, M. T., Onasch, T. B., Northway, M. J., Jayne, J. T., Canagaratna, M. R., Herndon, S. C., Wood, E. C., Miake-Lye, R. C., & Knighton, W. B. (2010). Gas turbine engine emissions—Part II: Chemical properties of particulate matter. *ASME Journal of Engineering for Gas Turbine and Power, 6*(132). https://doi.org/10.1115/1.4000132, 061505-061505-061515.

Vancassel, X., Mirabel, P., & Garnier, F. (2014). Numerical simulation of aerosols in an aircraft wake using a 3D LES solver and a detailed microphysical model. *International Journal of Sustainable Aviation, 2*(1), 139–159. https://doi.org/10.1504/ijsa.2014.065480

Wey, C. C., Anderson, B. A., Wey, C., Miake-Lye, R. C., Whitefield, P., & Howard, R. (2007). Overview on the aircraft particle emissions experiment (APEX). *Journal of Propulsion and Power, 5*(23), 898–905. https://doi.org/10.2514/1.26406

Wong, H.-W., Jun, M., Peck, J., Waitz, I. A., & Miake-Lye, R. C. (2014). Detailed microphysical modeling of the formation of organic and sulfuric acid coatings on aircraft emitted soot particles in the near field. *Aerospace Science and Technology, 9*(48), 981–995. https://doi.org/10.1080/02786826.2014.953243

Wong, H.-W., Jun, M., Peck, J., Waitz, I. A., & Miake-Lye, R. C. (2015). Roles of organic emissions in the formation of near field aircraft-emitted volatile particulate matter: A kinetic microphysical modeling study. *ASME Journal of Engineering for Gas Turbine and Power, 7*(137). https://doi.org/10.1115/1.4029366, 072606-072606-072610.

Wong, H. W., & Miake-Lye, R. C. (2010). Parametric studies of contrail ice particle formation in jet regime using microphysical parcel modeling. *Atmospheric Chemistry and Physics, 7*(10), 3261–3272. https://doi.org/10.5194/acp-10-3261-2010

Yu, F., Kärcher, B., & Anderson, B. E. (2024). Revisiting contrail ice formation: Impact of primary soot particle sizes and contribution of volatile particles. *Environmental Science and Technology, 40*(58), 17650–17660. https://doi.org/10.1021/acs.est.4c04340

Yu, Z., & Miake-Lye, R. C. (2024). Volatile contributions to aviation nvPM: A mass spectrometric analysis of nvPM emissions. *Meteorologische Zeitschrift, 1*(33), 5–14. https://doi.org/10.1127/metz/2024/1185

Yu, Z., Timko, M. T., Herndon, S. C., Miake-Lye, R. C., Beyersdorf, A. J., Ziemba, L. D., Winstead, E. L., & Anderson, B. E. (2019). Mode-specific, semi-volatile chemical composition of particulate matter emissions from a commercial gas turbine aircraft engine. *Atmospheric Environment, 218*. https://doi.org/10.1016/j.atmosenv.2019.116974, 116974-116974-116978.

Yu, F., Turco, R. P., & Kärcher, B. (1999). The possible role of organics in the formation and evolution of ultrafine aircraft particles. *Journal of Geophysical Research: Atmospheres, D4*(104), 4079–4087. https://doi.org/10.1029/1998JD200062